

# Evolution of the surface deformation profile and subsurface distortion zone during reverse faulting through overburden sand



Y.Y. Chang<sup>a</sup>, C.J. Lee<sup>a,\*</sup>, W.C. Huang<sup>a</sup>, W.Y. Hung<sup>a</sup>, W.J. Huang<sup>b</sup>, M.L. Lin<sup>c</sup>, Y.H. Chen<sup>d</sup>

<sup>a</sup> Department of Civil Engineering, National Central University, Taiwan

<sup>b</sup> Department of Applied Geology Engineering, National Central University, Taiwan

<sup>c</sup> Department of Civil Engineering, National Taiwan University, Taiwan

<sup>d</sup> Central Geological Survey, MOEA, Taiwan

## ARTICLE INFO

### Article history:

Received 8 May 2014

Received in revised form 16 October 2014

Accepted 21 October 2014

Available online 1 November 2014

### Keywords:

Distinct element method

Reverse faulting

Surface deformation profile

Subsurface distortion zone

Gompertz sigmoid function

Affected width

## ABSTRACT

The 2D distinct element method was used to investigate the propagation of fault rupture traces through overlying sand during reverse faulting along a range of dip angles and at different vertical throws. Calibrated micromechanical material parameters were used in the numerical simulations, which were validated through a comparison of the simulation results with those obtained from a centrifuge experiment involving acceleration at 80 g. The Gompertz sigmoid function with three parameters provided the best fit to the normalized surface deformation profiles obtained both from the numerical simulation and from centrifuge experiments. The three parameters that characterized the Gompertz sigmoid function were the normalized scarp height, the maximum slope on the scarp, and the location of the reverse fault outcropping. A surface deformation profile slope of 1/150 was used as the setback criterion. The normalized affected width and fault outcrop relative to the fault tip were determined for reverse faults having a variety of dips and throws. The dip angle significantly affected the kinematic mechanism underlying reverse faulting. At a given vertical throw, the scarp height increased as the dip angle decreased in the cases of  $\alpha < 45^\circ$ , and the scarp maintained a relatively constant height in the cases of  $\alpha > 45^\circ$ . As the dip angle decreased, the location of the fault outcropping shifted toward the footwall and the maximum slope on the scarp increased. The horizontal displacement played a significant role at low dip thrusts ( $\alpha = 22.5^\circ, 30^\circ, 37.5^\circ$ ), a back-thrust fault developed, and an inverted triangle wedge formed in the subsurface.

© 2014 Elsevier B.V. All rights reserved.

## 1. Introduction

Earthquakes induce two types of ground deformations. One such deformation arises from transient ground shaking waves that travel away from the rupture points on a fault and propagate over great distances in the earth. These waves have attracted significant attention in studies of the dynamic responses of soils and structures during ground oscillations. The second type of ground deformation involves permanent ground displacements during the complete (or near-complete) emergence of a fault rupture at the ground surface. Displacements of the overlying soil as a result of a dip-slip fault, including angular distortions and lateral ground strain, can introduce a tremendous amount of damage to man-made structures, especially if fault ruptures break the ground surface in urbanized areas. In 1999, three major earthquakes occurred in Kocaeli, Turkey, in Düzce, Turkey (Anastasopoulos et al., 2001), and in Chi-Chi, Taiwan (Chen et al., 2000; Dong et al., 2004). Numerous man-made structures were destroyed due to ground

displacements associated with fault rupture emergence at the ground surface. The ground surface and subsurface deformations caused severe damage to buildings, major infrastructure, tunnel, water and sewer utilities, electrical conduit systems, and power utilities (Lin et al., 2007). Fig. 1 shows the ground surface deformation profile measured on the sports field at the Guangfu Junior High School as a result of reverse faulting during the 1999 Chi-Chi Earthquake. This surface deformation profile is preserved in the 921 Earthquake Museum of Taiwan (<http://www.921emt.edu.tw>) as a lesson from the 921 Chi-Chi Earthquake disaster. In general, the surface displacements induced by normal or reverse faulting can be divided into two components: vertical uplift (or falling) and lateral offset at the ground surface. Man-made structures or piping utilities in close proximity to a rupture zone on the ground surface or embedded in the subsurface distortion zone can suffer severe damage. One approach to preventing damages to man-made structures is to avoid building structures near a fault-induced affected zone on the ground surface or in subsurface distortion zones. For example, setback distances of 50 ft (15.3 m) in California (Bryant and Hart, 2007; Borchardt, 2010) or 30–50 m in Taiwan are typically imposed on either side of a fault trace. Prior to establishing appropriate setback widths for active faults or adopting geotechnical mitigation strategies in relation to surface ruptures, it is important to assess the

\* Corresponding author at: Department of Civil Engineering, National Central University, No. 300, Jhongda Rd., Jhongli City, Taoyuan County 32001, Taiwan. Tel.: +886 3 4227151x34135; fax: +886 3 4252960.

E-mail address: [cjleeciv@ncu.edu.tw](mailto:cjleeciv@ncu.edu.tw) (C.J. Lee).



Fig. 1. Ground surface deformation induced by the reverse fault slip in the 1999 Chi-Chi earthquake (provided by W.J. Huang, NCU).

following: (1) the propagation of a fault trace from the bedrock through the overburden soil to the ground surface; (2) the location at which a rupture trace emerges on the ground surface; (3) the full extent of the surface deformation profile and the significant subsurface distortion zone; and (4) the changes in slope on the surface deformation profile and the height of a scarp in relation to the base rock displacement.

Three research approaches have been applied toward evaluating rupture propagation through overburden soil under normal and reverse faulting: field investigations involving trial trench excavations (Bray et al., 1994a; Chen et al., 2007), numerical simulations (Bray et al., 1994b; Lin et al., 2006; Anastasopoulos et al., 2007; Loukidis et al., 2009; Abe et al., 2011; Taniyama, 2011; Nollet et al., 2012; Mortazavi Zanjani and Soroush, 2013), and semi-analytical methods (Anastasopoulos et al., 2008), and 1 g ( $g = 9.8 \text{ m/s}^2$ ) involving sandbox model tests (Cole and Lade, 1984; Lin et al., 2006; Fadaee et al., 2013) or centrifuge physical modeling (Lin et al., 2005; Bransby et al., 2008a, 2008b; Ng et al., 2012; Chang et al., 2013). Field case histories after earthquakes usually provide the most reliable information about the mechanisms through which fault events occurred; however, it is not easy to survey the extent of variability through field studies, and it is impossible to perform a detailed parametric analysis. Numerical simulations and/or physical modeling experiments, on the other hand, can provide efficient parametric study methods. Numerical simulations can be used to perform ensemble simulations without significant effort, with the exception of the computational time spent. Even in computational approaches, the assignment of appropriate constitutive relations in finite element methods or finite difference methods, or the assignment of the microscopic mechanical properties of a material in distinct element methods, remains challenging. Physical modeling studies can explore the kinematic and failure mechanisms underlying fault rupture and can validate numerical simulation results. Hence, both physical experiments and numerical simulations are conducted in attempts to relate numerical simulation and physical experiment results (Anastasopoulos et al., 2007; Ng et al., 2012). Once validated, the model geometry and boundary conditions in a numerical simulation may be varied to study the behavior associated with normal and reverse faulting.

The distinct element method has several advantages in its ability to address fault rupture propagation problems. The distinct element technique is well suited for modeling the development of discontinuities or overburden soil deformations under large strains (i.e., shear bands,

faults). In addition, this technique can model deformations involving unlimited relative motions of individual elements or complex boundary conditions (Cundall and Strack, 1979). The main goal of this paper is to investigate, using numerical simulations implemented in the Particle Flow Code (PFC<sup>2D</sup>), the evolution of surface deformation profiles and the propagation of subsurface rupture traces induced by reverse faulting along various dip angles through overlying sand. The numerical simulations were verified through a comparison to a centrifuge model of the surface and subsurface deformation profiles during reverse faulting at a dip angle of 60°, which provided confidence in the validity of the numerical results (PFC<sup>2D</sup>). The calculated surface deformation profiles and fault rupture traces during reverse faulting at various dip angles are presented as guidelines for specifying setback zone widths within which civil construction should be either disallowed or require specialized designs. Fig. 2 shows the coordinate system and geometry of the overburden soil layer and the fault tip of a reverse fault and the problem studies herein. A soil deposit of thickness  $H$  overlies a reverse fault with a dip angle of  $\alpha$  relative to the horizontal. The upward vertical

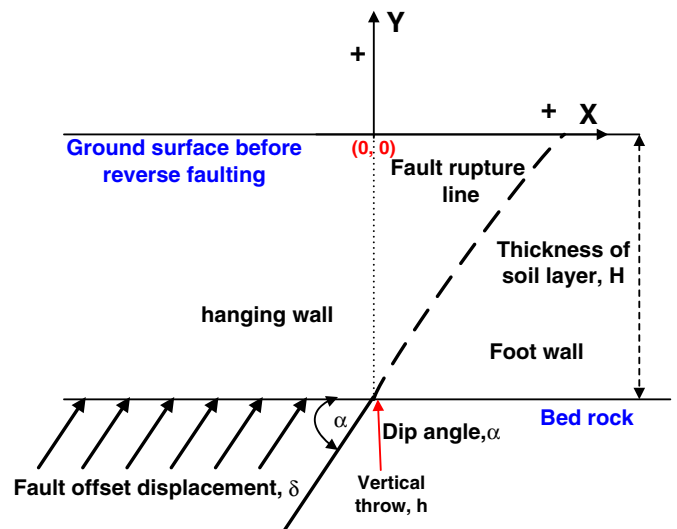


Fig. 2. Definition of the coordinate system and the geometry of overburden soil layer and the fault tip of the reverse fault.

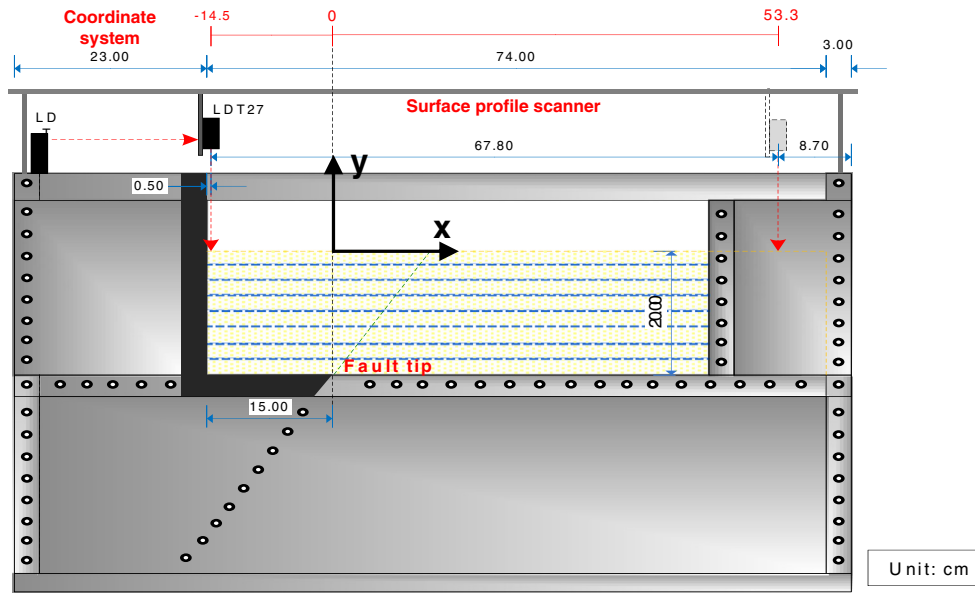


Fig. 3. Dimensions of the fault simulation container and the coordinate system used in the centrifuge experiments.

displacement (positive) of the reverse fault at the bed rock is denoted by vertical throw,  $h$ , and the ratio of the vertical throw to the thickness of overburden soil,  $r$  (%), is defined as

$$r(\%) = \frac{h}{H} \times 100. \quad (1)$$

## 2. Geotechnical Centrifuge modeling

### 2.1. Testing equipment

The experiments in this study were undertaken at the beam centrifuge at the National Central University (NCU), Taiwan. The NCU Geotechnical Centrifuge has a nominal radius of 3 m and integrates a 1D servo-hydraulically controlled shaker with a swing basket. The maximum payload of the platform is 400 kg at an acceleration of 80 g (Lee et al., 2011).

A fault simulation container having dimensions 1000 mm × 528 mm × 675 mm (length × width × height) was designed for the reverse fault test with a dip angle of 60°. A volume 740 mm in length,

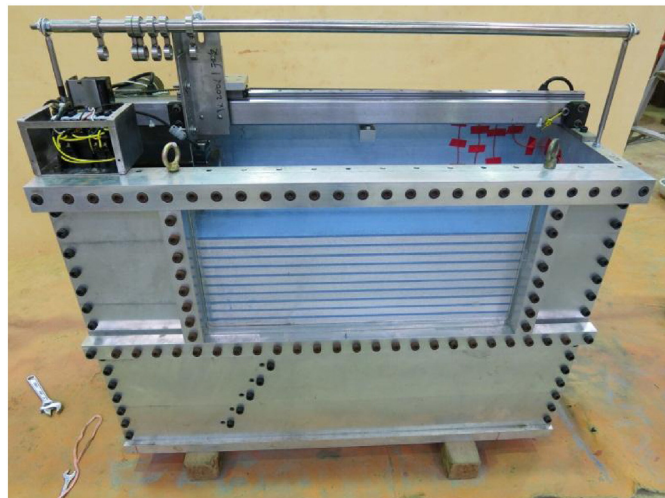


Fig. 4. Photo of fault simulation container equipped with a surface profile scanner.

300 mm in width, and 325 mm in height was provided for the tested soil bed in the container. An acrylic window 600 mm × 281.5 mm in area was used to observe the subsurface deformation profiles during reverse faulting. The container simulated a fault slip with a speed of 0–2.5 mm/min in a displacement control mode. The maximum vertical throw reached 55 mm. An in-flight surface profile scanner equipped with two laser displacement transducers installed horizontally and vertically and driven with a motor with a sampling rate of 100 samples/s densely scanned the surface elevations on the center line of the tested sand bed during faulting tests. Fig. 3 shows the dimensions of the fault simulation container and the coordinate system used to demonstrate the testing results, as discussed in the following sections. As shown in Fig. 3, the origin of the coordinate system was the point at which the fault tip vertically projected onto the ground surface. Fig. 4 shows a photograph of the fault simulation container equipped with a surface profile scanner.

### 2.2. Tested sand, sand bed preparation, and testing conditions

Crushed quartz sand was used to prepare the uniform sand bed for all tests conducted in this study. The fine uniform silica sand was characterized by  $D_{50} = 0.149$  mm,  $\rho_{max} = 1660$  kg/m<sup>3</sup>, and  $\rho_{min} = 1380$  kg/m<sup>3</sup>. Fig. 5 shows the grain size distribution of the tested sand. A peak friction angle of  $\phi_{peak} = 41^\circ$  and a dilation angle of  $\phi = 6^\circ$  were measured using a direct shear test for sand with a relative density of 70% at a normal stress = 200 kPa. The dry quartz sand was pluviated

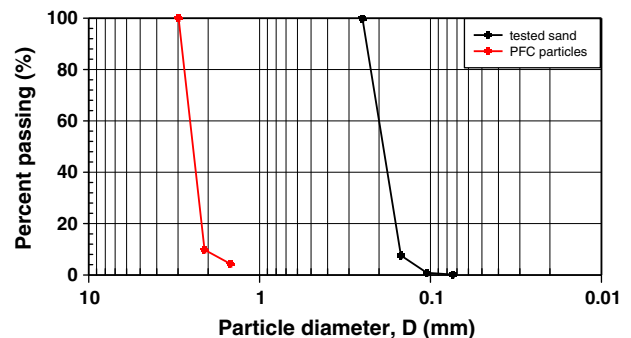


Fig. 5. Grain size distribution curves of disks used in PFC<sup>2D</sup> numerical modeling and the tested sand used in centrifuge modeling.

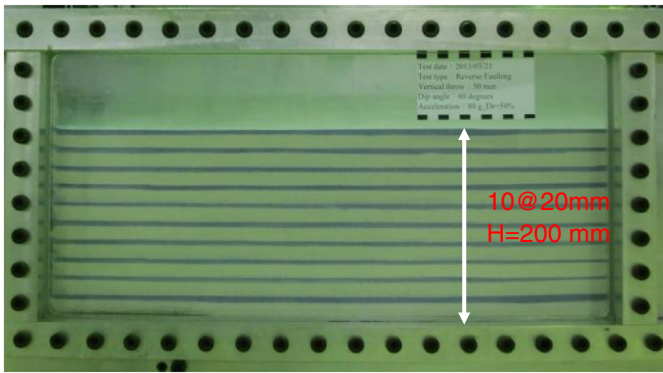


Fig. 6. Photo of prepared testing sand bed before reverse faulting.

from a hopper along a regular path into the container at a specified falling height and a constant flow rate to prepare a fairly uniform sand deposit with a relative density of approximately 70%. The pluviation process was interrupted as needed to spray a thin layer of blue dyed sand at specified elevations as marker layers in proximity to the acrylic window to allow identification of shear deformations in the subsurface, as shown in Fig. 6. A sand bed 200 mm thick ( $H$ ) was prepared to correspond to 16 m on the prototype scale when tested at an acceleration of 80  $g$ .

The centrifuge was accelerated at an acceleration of 10  $g$  per step until it reached the target acceleration (80  $g$ ). In each step, the surface profile scanner was triggered to scan the surface profile and measure the surface settlements caused by the high  $g$  levels. The settlement behavior of the sand bed confined in the fault simulation container was stressed under at-rest conditions (the  $k_o$  condition). The constrained modulus,  $M_{physical}$ , of the tested sand under plane strain conditions was defined as

$$M_{physical} = \frac{\sigma'_v}{\epsilon_v} = \frac{1-\nu}{(1+\nu)(1-2\nu)} E \quad (2)$$

where  $\sigma'_v$  is the effective overburden stress,  $\epsilon_v$  is the vertical strain,  $E$  is the Young's modulus, and  $\nu$  is Poisson's ratio. The average constrained modulus of the sand bed under various stress states (corresponding to different  $g$  levels) could be calculated using Eq. (2). The value of  $M_{physical}$  depended on the value of the effective overburden stress. The empirical relationship between the average constrained modulus and the stress levels could be formulated as follows:

$$M_{physical} = B(\sigma'_v)^m \text{ (kPa)} \quad (3)$$

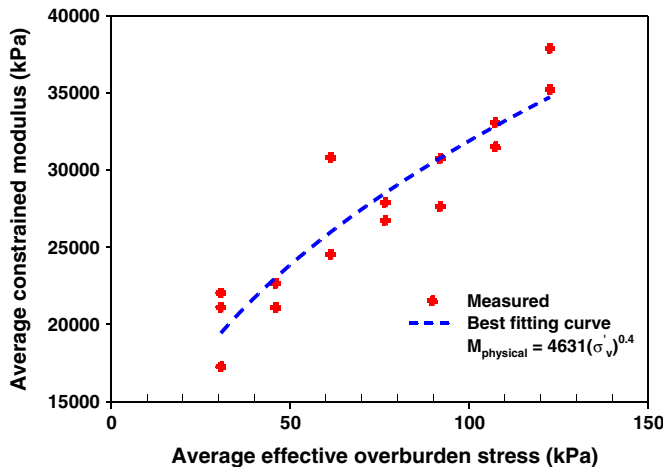


Fig. 7. Empirical relation of the measured constrained modulus and the average effective overburden stress in the self-weight consolidation stages in the centrifuge experiment.

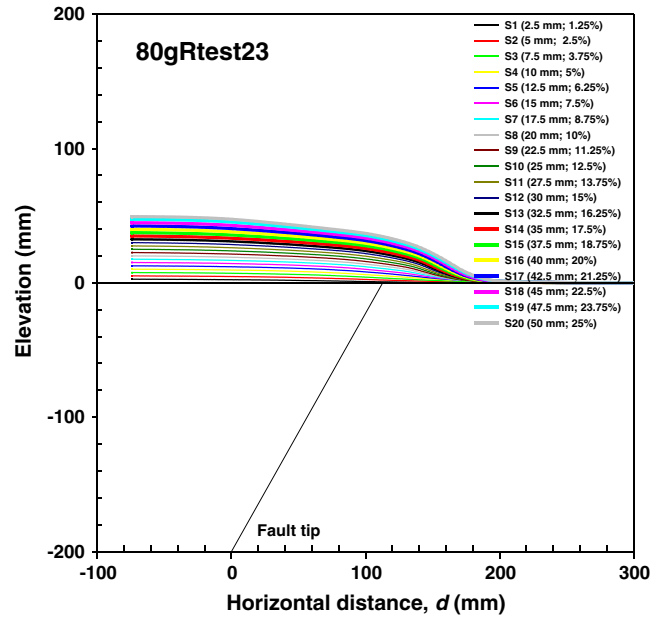


Fig. 8. Surface deformation profiles at various throws for reverse faulting (both dimensions in model scale).

where  $B = 4631$  and  $m = 0.4$  produce the best curve fitting results for the tested sand bed, as shown in Fig. 7.

Once the centrifuge reached the target acceleration (80  $g$ ), reverse faulting was conducted. The fault throw was increased at a constant velocity of 2 mm/min using an AC motor. The surface profile scanner was driven once to scan the surface elevations per 2.5 mm throw increment. The fault slip displacement increased until reaching a final throw of 50 mm ( $r = 25\%$ , corresponding to a vertical throw of 4 m at the prototype scale). In total, 20 scans were performed (S1–S20;  $r = 1.25\%–25\%$ ) to measure the evolution of the ground surface profile during the reverse fault tests.

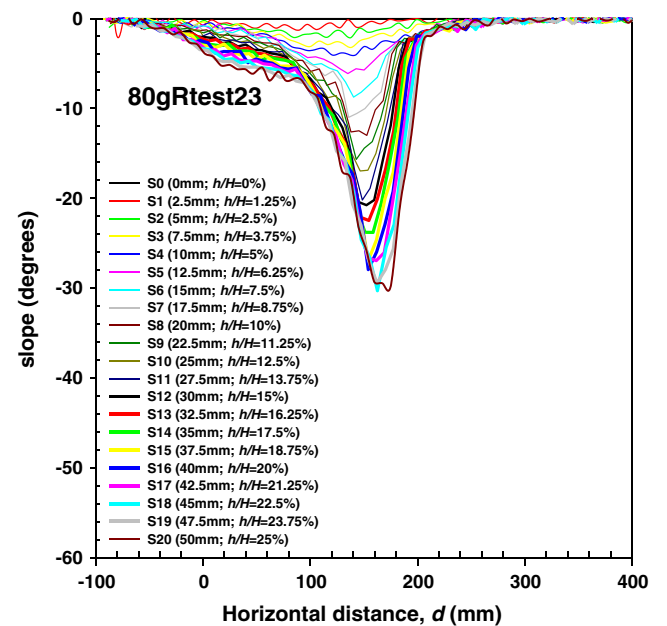


Fig. 9. Slopes of the surface deformation profiles at various throws for reverse faulting (dimensions in model scale).

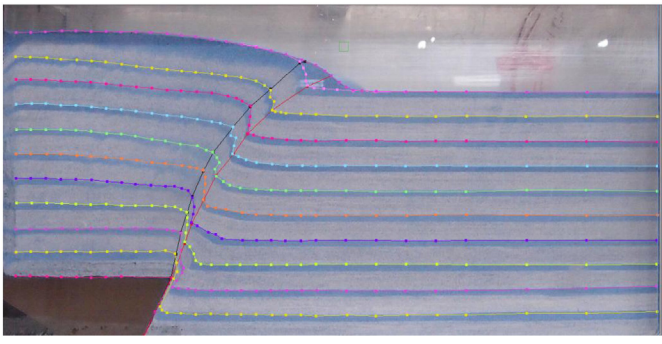


Fig. 10. Digitization on the image of subsurface deformation profile after 50-mm-throw reverse faulting.

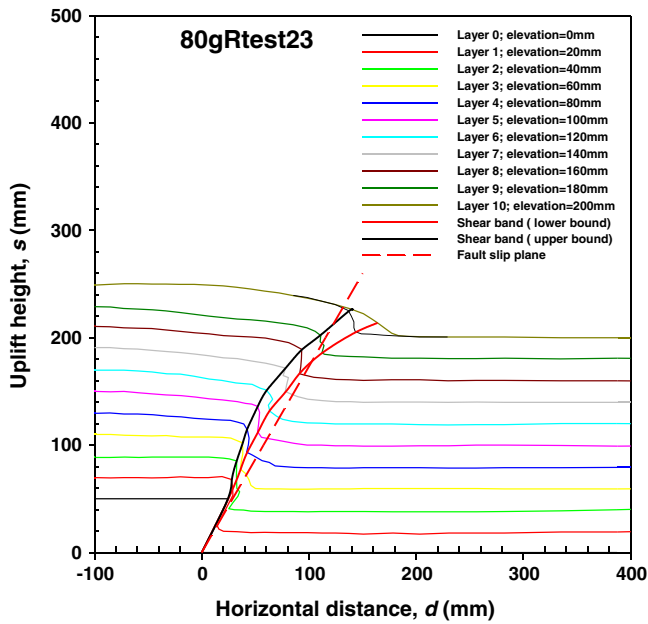


Fig. 11. Major shear-induced distortion zone after 50-mm-throw reverse faulting.

2.3. Test results and interpretations of the centrifuge reverse fault experiment

Fig. 8 displays the surface deformation profiles (uplift height,  $s$ , versus horizontal distance,  $d$ , from the fault tip) at various throws (ranging from  $r = 1.25\%$  to  $r = 25\%$ ) and the relative positions of the surface deformation profiles relative to the fault tip on the bed rock (both dimensions are provided in the model scale), respectively. As expected,

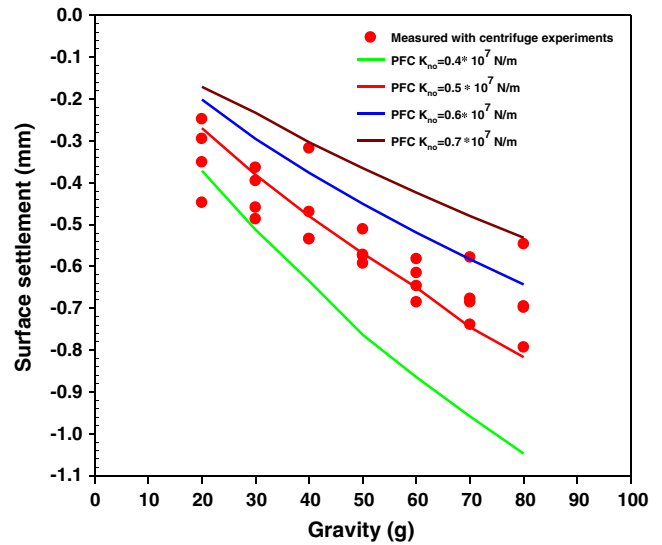


Fig. 13. Comparison between the surface settlements calculated with various  $K_{110}$  in the numerical simulations and the measured surface settlements from the centrifuge experiments at corresponding  $g$ -levels.

the uplift height increased as the vertical throw increased. Fig. 9 shows the calculated slopes on the surface deformation profiles at various throws. The slope profile at various throws followed an asymmetrical bell-shaped curve. The values at which the peak positions occurred in the curves increased as the vertical throw increased, and the peaks of the bells simultaneously and gradually shifted toward to the footwall.

Fig. 10 shows a photograph of the subsurface deformation profiles collected from the acrylic window after the reverse fault test ( $h = 50\text{ mm}$ ;  $r = 25\%$ ). The 10 thin blue colored sand marker layers in the soil bed provided a good visual picture of the rupture pattern after testing. A digitizer was used to trace and mark the deformation shapes (colored lines with dots as shown in Fig. 10) in each soil layer. The rupture paths of each soil layer were connected to plot two major rupture paths, and the distortion zone between the two major paths could be identified. Digitizer software was then used to convert the selected points on the image of the subsurface deformation profile into digital representations. The fault rupture lines and their relative positions could then be converted into a digital format for digital processing and management. Fig. 11 shows the upper bound (black line) and the lower bound (red line) of the rupture path, which were obtained by connecting the points corresponding to the minimum radii of curvature in each marker layer. These rupture paths initially extended along the dip plane and then curved out over the footwall. The zone confined within the upper and lower bounds constituted the major

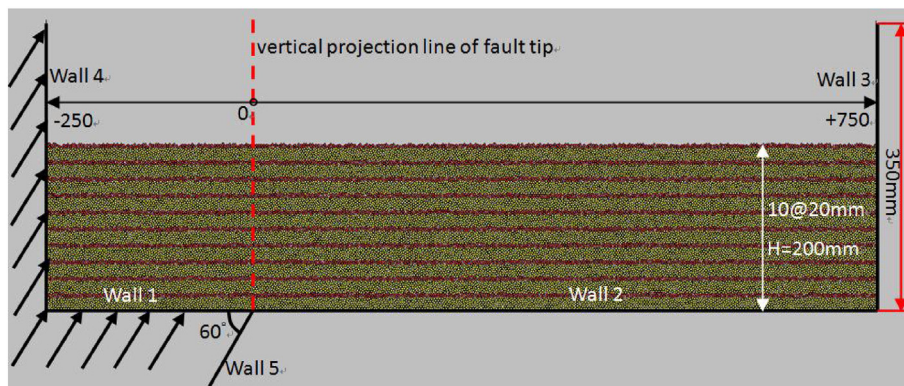


Fig. 12. Dimensions of numerical grain assembly used in PFC<sup>2D</sup> numerical simulation.

faulting-induced distortion zone. This major distortion zone was defined as the shear band induced by reverse faulting.

### 3. Distinct element modeling methodology

#### 3.1. Preparation of the numerical grain assembly used for the PFC<sup>2D</sup> calculations

The PFC<sup>2D</sup> suite is a 2D distinct element software algorithm for simulating the mechanical behavior of granular assemblies. This study used the PFC<sup>2D</sup> to analyze the phenomenon of reverse fault rupture propagation from base rock through an overlying sand layer to the ground surface. The simulations took advantage of a linear contact model and a slip model defined by the normal and shear stiffness  $K_n$  and  $K_s$ , and the friction coefficient at the contact plane,  $\mu$ , for two contact entities (ball-to-ball and ball-to-wall). The numerical simulation domain was defined as having five rigid walls (Wall 1, Wall 2, Wall 3, Wall 4, and Wall 5), as shown in Fig. 12. The distance from Wall 3 to Wall 4 was 1000 mm, longer than the length of the test sand bed (740 mm) used in the centrifuge experiments. The use of a longer system in the numerical analysis allowed us to conduct numerical simulations of fault rupture events using small dip angles ( $<60^\circ$ ) and avoided the potential for boundary effects from the walls. Wall 2 and Wall 3 were fixed walls, and Wall 1, Wall 4, and Wall 5 moved along a vector aligned with the predetermined fault rupture plane.

The numerical grain assembly used in the numerical simulation of PFC<sup>2D</sup> consisted of 28,759 circular disks with three radii: 1.49 mm, 1.05 mm, and 0.74 mm. The grain size distribution of circular disks used in the PFC<sup>2D</sup> numerical modeling is parallel to that of tested sand as shown in Fig. 5. The mean grain size,  $D_{50}$ , of circular disks is 2.41 mm, which is approximately 16 times larger than that of the tested sand. The numerical grain assembly was constructed by randomly pluviating mixed disks into a box confined by 4 walls in a layer-by-layer manner. Each 20 mm thick layer consisted of 1578 mixed disks, and 50 thin layers were initially stacked. The stacked layers were then subjected to 1 g self-weight consolidation until the average unbalanced force ratio was less than 0.01. Disks positioned at heights exceeding 200 mm were removed to form the final numerical grain assembly 200 mm in thickness. Fig. 12 shows the dimensions of the numerical grain assembly and the coordinate system used to demonstrate the numerical results described in the following sections. The position of the reverse fault tip was defined as the origin of the x-axis in the coordinate system. The direction to the right was defined as the positive direction, and the left was defined as the negative direction. This coordinate system was used in both the PFC<sup>2D</sup> simulations and in the centrifuge experiments, to facilitate a comparison of results. The disks at elevations of approximately 2, 4, 6, 8, 10, 12, 14, 16, 18, and 20 mm were marked with red to form marker layers, and the positions of these disks were continuously traced during simulations of the reverse faulting events. This prepared grain assembly was used to numerically analyze the reverse faulting events.

#### 3.2. Procedures used in the PFC<sup>2D</sup> numerical simulations

The micromechanical material input parameters used in PFC<sup>2D</sup> analysis included the normal and shear stiffnesses of the disks,  $K_n$  and  $K_s$ , the normal and shear stiffnesses of the walls,  $K_{nw}$  and  $K_{sw}$ , the density of disks,  $\rho$ , and the friction coefficient,  $\mu$ , between the disks and between a disk and a wall. The micromechanical material parameters were calibrated prior to performing the numerical simulation. The calibration methodology and procedure proposed by Chang et al. (2013) were used to determine the micromechanical properties of the PFC<sup>2D</sup> system. The methodology was based on a comparison of the surface settlements measured in the numerical grain assembly, calculated using PFC<sup>2D</sup> numerical simulations of the self-weight consolidation stage between 1 g and 80 g, with the surface settlements measured from the tested

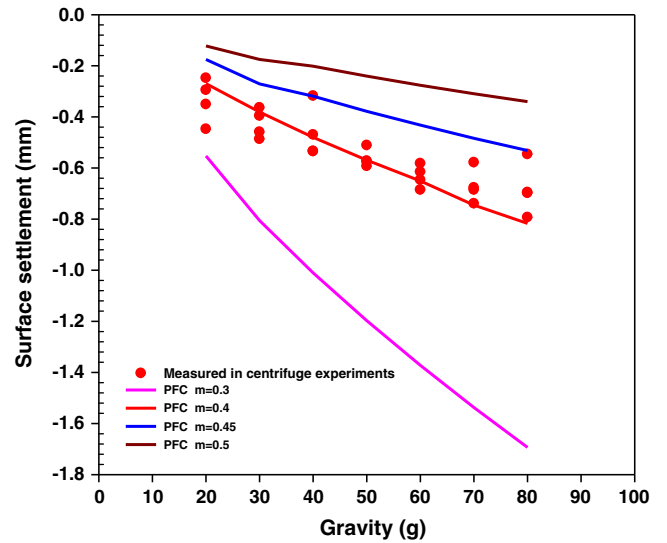


Fig. 14. Comparison of the surface settlements calculated with  $K_{no} = 0.5 \times 10^7$  N/m and various  $m$  ( $m = 0.3, 0.4, 0.45, \text{ and } 0.5$ ) in the numerical simulations and the measured surface settlements from the centrifuge experiments at corresponding  $g$ -levels.

sand bed during the centrifuge experiment between accelerations at 1 g and 80 g. The PFC<sup>2D</sup> numerical simulation procedures may be summarized as follows:

- (1) Calibration of the micromechanical material parameters.

The micromechanical stress–strain model based on a micro-mechanics theory of isotropic granular materials proposed by Yimsiri and Soga (2000) describes the relationship between the macroscopic parameters  $E$  and  $\nu$  and the microscopic material parameters ( $K_n, K_s, r, N$ , and  $V$ ) for an isotropic granular assembly:

$$E = \frac{4r^2N}{9V} \left[ \frac{15K_nK_s}{2K_n + 3K_s} \right] = \frac{4r^2N}{9V} \left[ \frac{15K_n}{2\frac{K_n}{K_s} + 3} \right] \quad (4)$$

$$G = \frac{4r^2N}{9V} \left[ \frac{15K_nK_s}{6K_n + 4K_s} \right] = \frac{4r^2N}{9V} \left[ \frac{15K_n}{6\frac{K_n}{K_s} + 4} \right] \quad (5)$$

$$\nu = \frac{5(K_n - K_s)}{10K_n + 3K_s} = \frac{\frac{K_n}{K_s} - 1}{2\frac{K_n}{K_s} + 3} \quad (6)$$

where  $r$  is the radius of the particle,  $N$  is the coordinate number of a particle, and  $V$  is the volume of the assembly. Eq. (6) shows that

Table 1  
Representative micro-mechanical parameters used in PFC<sup>2D</sup> numerical simulation.

| Parameters                                  | Values   |
|---|--|
| Normal stiffness, $K_n$ (N/m)               | $K_n = 0.5 \times 10^7 \left( \frac{\sigma'_v}{\sigma'_v} \right)^{0.4}$ |
| Shear stiffness, $K_s$ (N/m)                | $1/3K_n$   |
| Normal stiffness of walls (N/m)             | $6.0 \times 10^{12}$   |
| Shear stiffness of walls (N/m)              | $6.0 \times 10^{12}$   |
| Friction coefficient between disks          | 0.73 ( $\varnothing = 36^\circ$ )  |
| Friction coefficient between disks and wall | 0.0  |
| Density of disks (kg/m <sup>3</sup> )       | 1850   |
| Local damping coefficient                   | 0.7 (default)  |

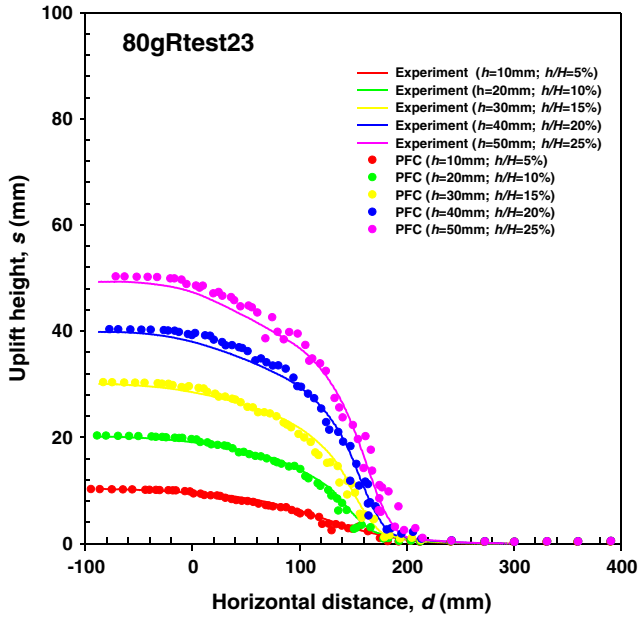


Fig. 15. Comparison of the surface deformation profiles calculated from the PFC<sup>2D</sup> simulation and those obtained measured from the centrifuge experiment under the condition of 80 g.

$v$  depended only on the ratio of the normal stiffness to the shear stiffness,  $K_n/K_s$ . The settlement of the numerical grain assembly confined by the walls during the self-weight consolidation stage (as the  $g$  level was increased) was stressed under at-rest conditions ( $k_o$  conditions). The coefficient of the earth pressure at rest,  $k_o$ , was related to the effective friction angle,  $\phi'$ , according to the following formula:

$$k_o \approx (0.95 - \sin \phi'). \quad (7)$$

The sand in the stress state of the at-rest condition did not display failure and could represent a state of elastic equilibrium. Therefore, the coefficient of earth pressure at rest may be represented using Poisson's ratio, expressed as

$$k_o = \frac{v}{1-v} \quad (8-a)$$

and

$$v = \frac{k_o}{1+k_o}. \quad (8-b)$$

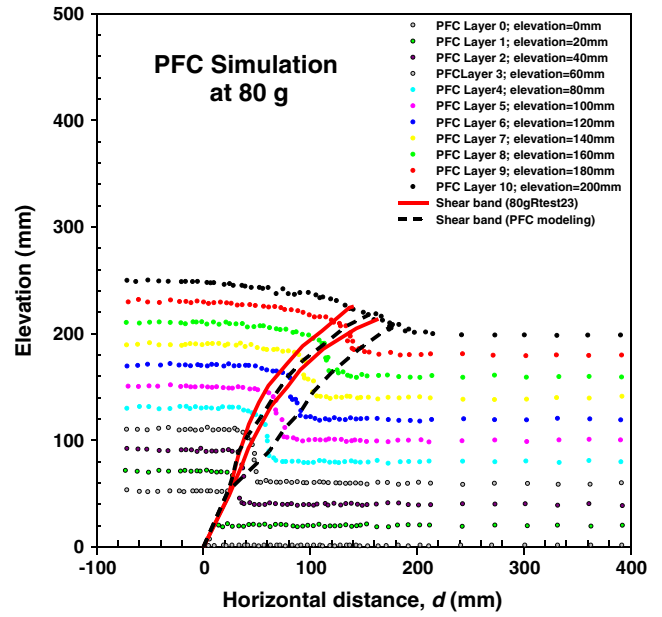


Fig. 17. Final displacement patterns of the marked layers and the comparison of the major faulting-induced distortion zone in the numerical grain assembly and experiment test simulated under the condition of 80 g.

The effective internal friction angle of the tested sand, ( $\phi_{peak}$ ), was equal to  $41^\circ$ , leading to  $k_o = 0.294$  (Eq. (7)) and  $v = 0.227$  (Eq. (8-b)). Substituting  $v = 0.227$  into Eq. (6), the ratio of the normal stiffness to the shear stiffness ( $\frac{K_n}{K_s}$ ) becomes 3.07. We therefore assumed a value of  $\frac{K_n}{K_s} = 3$  in the study presented here. The measured  $M_{physical}$  could be used to calibrate the value of  $K_n$  used in the PFC<sup>2D</sup> analysis. The measured constrained modulus increased as the effective overburden stress in the centrifuge model increased. We therefore assumed that the normal stiffness increased with the effective overburden stress,  $\sigma'_v$  in both the experimental and the numerical grain assembly. The relationship between  $K_n$  and  $\sigma'_v$  could be expressed as

$$K_n = K_{no} \left( \frac{\sigma'_v}{\sigma'_{v0}} \right)^{0.4} \quad (9)$$

where  $\sigma'_{v0}$  is the effective overburden stress at a depth of 1 cm for the numerical grain assembly under 1 g conditions and  $K_{no}$  is the normal stiffness under a stress of  $\sigma'_{v0}$ . Therefore, the normal

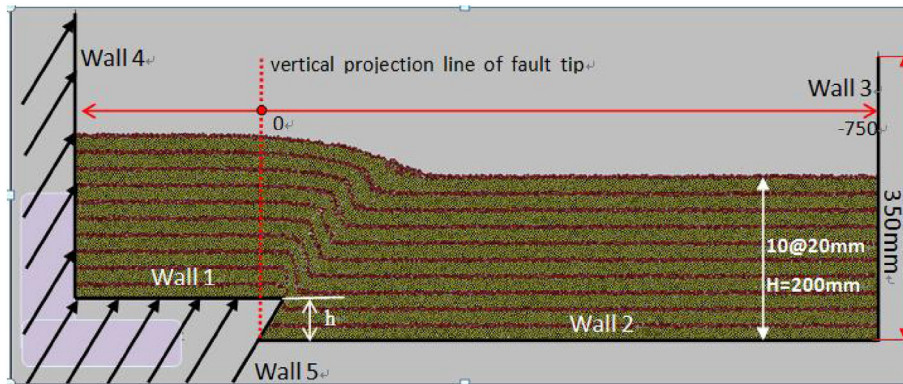


Fig. 16. Final subsurface displacement pattern of the marked layers in the numerical grain assembly after being subjected to the 50 mm vertical throw ( $r = 25\%$ ) with the  $60^\circ$  dip angle reverse faulting in the numerical grain assembly under the condition of 80 g.

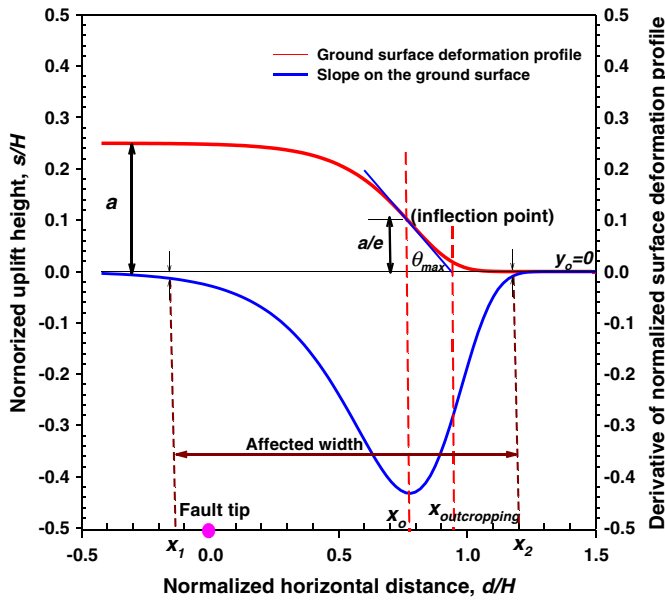


Fig. 18. Gompertz function and coordinate system used to model the normalized surface deformation profile and the slopes on the profile.

stiffness of the contact at different depths and at different  $g$  levels could be assigned. The peak friction angle of the granular material could be represented as the sum of the sliding resistance at a contact, particle rearrangements, and dilation. This study used a numerical grain assembly to simulate the shear behavior of the sand deposit ( $Dr = 70\%$ ) characterized by  $\phi_{peak} = 41^\circ$  and a dilation angle of  $\psi = 6^\circ$ . Therefore, the friction coefficient between disks,  $\mu$ , was assumed to be equal to 0.73.

After determining the ratio of the normal and shear stiffness ( $\frac{K_n}{K_s} = 3$ ), the friction coefficient ( $\mu = 0.73$ ), and  $m = 0.4$  used in Eq. (9), a series of preliminary PFC<sup>2D</sup> numerical simulations using various normal stiffness values ( $K_{no} = 0.4 \times 10^7$ ,

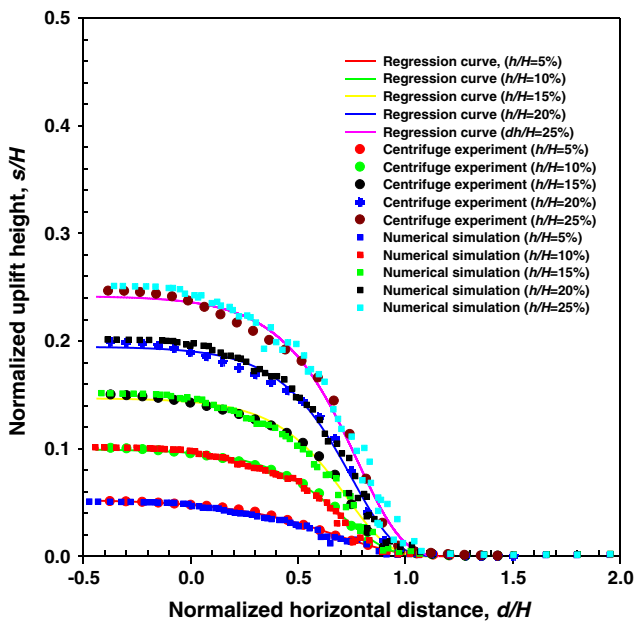


Fig. 19. Comparison of the prediction of Gompertz function and the results obtained from the centrifuge experiment and those from the PFC<sup>2D</sup> numerical simulation (dip angle = 60°).

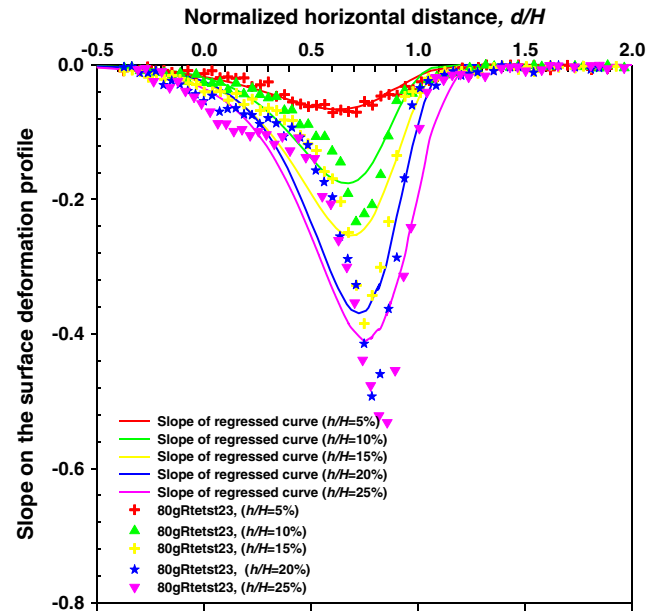


Fig. 20. Comparison of slopes on the normalized surface deformation profiles between the prediction and the results of the centrifuge experiment at different throws (dip angle = 60°). (a) Predicted normalized surface deformation profiles at different dip angles ( $r = 25\%$ ). (b) Predicted slopes on the profiles ( $r = 25\%$ ).

$0.5 \times 10^7$ ,  $0.6 \times 10^7$ , and  $0.7 \times 10^7$  N/m) was iteratively performed to calibrate the value of  $K_{no}$ . The numerical grain assembly was subjected to self-weight consolidation at each  $g$  level (from 1  $g$  to 80  $g$  in 10  $g$  increments). The surface settlements in the numerical grain assembly at different  $g$  levels were then calculated. Fig. 13 shows a comparison of the surface settlements calculated using the various values of  $K_{no}$  and the surface settlements measured from the centrifuge experiments at the corresponding  $g$  levels. Fig. 14 shows a comparison of the calculated surface settlements using  $K_{no} = 0.5 \times 10^7$  N/m, various values of  $m$  ( $m = 0.3, 0.4, 0.45$ , and  $0.5$ ), and the surface settlements measured from the centrifuge experiments at the corresponding  $g$  levels. Applying  $K_{no} = 0.5 \times 10^7$  N/m and  $m = 0.4$  in the PFC<sup>2D</sup> simulation produced results that were consistent with the settlements measured from the centrifuge models. Hence, the numerical grain assembly simulated using the PFC<sup>2D</sup> algorithm applied to the micromechanical parameters listed in Table 1 was capable of simulating the self-weight consolidation behaviors and the subsequent reverse faulting for the sand tested in the centrifuge experiments.

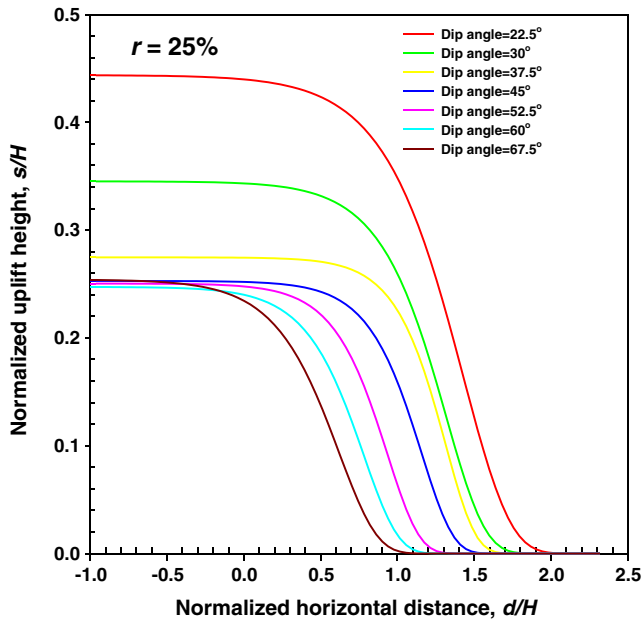
(2) Numerical simulations of reverse faulting events.

Numerical grain assembly simulated using the calibrated parameters listed in Table 1 were first subjected to self-weight consolidation under 80  $g$ . The systems were then subjected to a reverse

Table 2  
Characteristic parameters of normalized surface deformation profile at different dip angles and in the case of  $r = 25\%$ .

| Dip angle ( $\alpha$ )° | $a$    | $b$     | $x_o$  | $\theta_{max}$ (°) | $x_{outcropping}$ |
|-------------------------|--------|---------|--------|--------------------|-------------------|
| 22.5                    | 0.4432 | -0.3042 | 1.4293 | -28.19             | 1.7335            |
| 30                      | 0.3433 | -0.2598 | 1.3186 | -25.93             | 1.5784            |
| 37.5                    | 0.2715 | -0.1896 | 1.3229 | -27.78             | 1.5125            |
| 45                      | 0.2531 | -0.2063 | 1.1412 | -24.29             | 1.3475            |
| 52.5                    | 0.2504 | -0.2018 | 0.9189 | -24.54             | 1.1207            |
| 60                      | 0.2493 | -0.2239 | 0.7746 | -22.28             | 0.9985            |
| 67.5                    | 0.2545 | -0.2461 | 0.6098 | -20.83             | 0.8559            |

(a) Predicted normalized surface deformation profiles at different dip angles ( $r=25\%$ )



(b) Predicted slopes on the profiles ( $r=25\%$ )

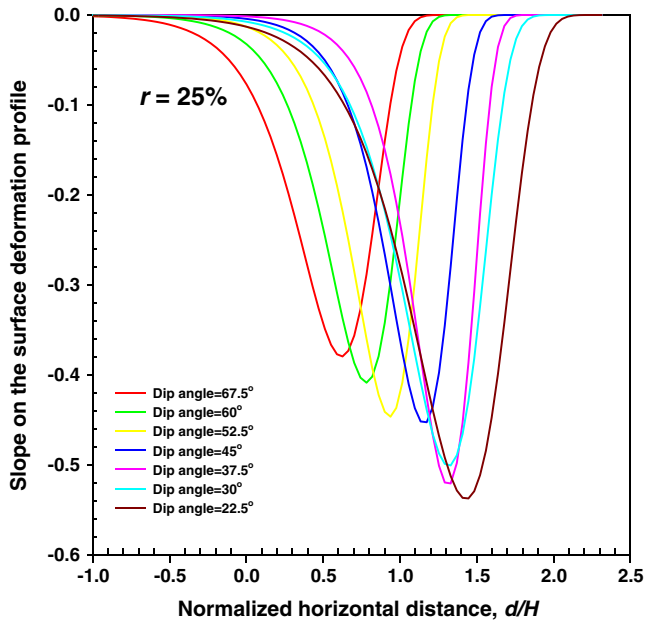


Fig. 21. Predicted normalized surface deformation profiles and their slopes on the profile at different dip angles in the case of  $r = 25\%$ : (a) predicted normalized surface deformation profiles; (b) predicted slopes on the profiles.

faulting event in which the moving Walls 1, 4, and 5 were uplifted along various directions at the fault dip angle ( $22.5^\circ$ ,  $30^\circ$ ,  $37.5^\circ$ ,  $45^\circ$ ,  $52.5^\circ$ ,  $60^\circ$ ,  $67.5^\circ$ ). The walls moved at a specified velocity of 2 mm/min. The surface deformation profiles were then monitored at vertical throws of 10, 20, 30, 40, and 50 mm. The subsurface deformation patterns and the rupture propagation of the reverse faulting from the base rock through the overlying sand to the ground surface were observed in detailed.

3.3. Validation of the PFC<sup>2D</sup> numerical simulation of reverse faulting at a  $60^\circ$  dip angle

The capabilities of the PFC<sup>2D</sup> numerical simulation method were verified by reproducing the reverse faulting behavior from the bedrock through the overlying sand to the ground surface. Numerical simulations of a  $60^\circ$  dip angle reverse faulting event were conducted. The surface deformation profiles in the numerical simulations and experimental results at different vertical throws were compared, as shown in Fig. 15. The numerical results agreed well with those measured from the centrifuge experiment. Fig. 16 presents the final subsurface displacement patterns of the marked layers measured in the numerical grain assembly after subjecting the test bed to a 50 mm vertical throw ( $r = 25\%$ ) with a  $60^\circ$  reverse faulting dip angle, under the condition of 80 g. This detailed subsurface distortion pattern resembled that obtained from the centrifuge experiments (Figure 10) and the field investigations involving trenching at the Chushan Excavation Site, Taiwan (Chen et al., 2007). The circular symbols shown in Fig. 17 represent the final elevations of the marked layers at various elevations. The major faulting-induced distortion zone derived from the numerical simulations (represented by dashed black lines) was established using the procedure that had been applied toward analyzing the experimental images (Figure 10). Fig. 17 shows that the extents of the major faulting-induced distortion zone obtained from the numerical simulations and centrifuge modeling were quite similar. Thus, the PFC<sup>2D</sup> algorithm associated with the proposed method for calibrating the material parameters could reasonably predict the surface deformation profiles at various vertical throws and provide a reasonable estimate of the subsurface distortion zone during a  $60^\circ$  dip angle reverse faulting event.

4. Functional of surface deformation profiles

The normalized surface deformation profile for reverse faulting is constructed from the surface deformation profile (uplift height,  $s$ , with respect to horizontal distance from the fault tip,  $d$ ) normalized by the thickness of soil deposit,  $H$ . Hence the normalized surface deformation profile is described as the normalized uplift height,  $s/H$ , with respect to the normalized horizontal distance,  $d/H$ . A Gompertz

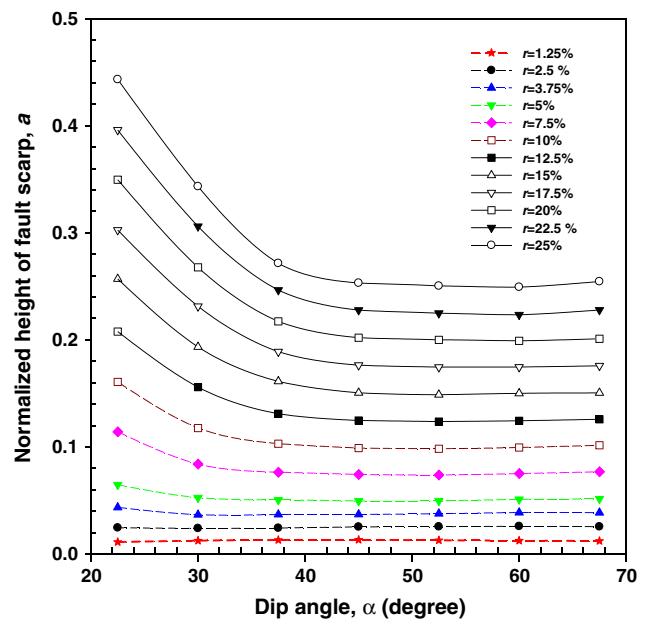


Fig. 22. Relations of normalized scarp height with the dip angles at various ratios of vertical throw.

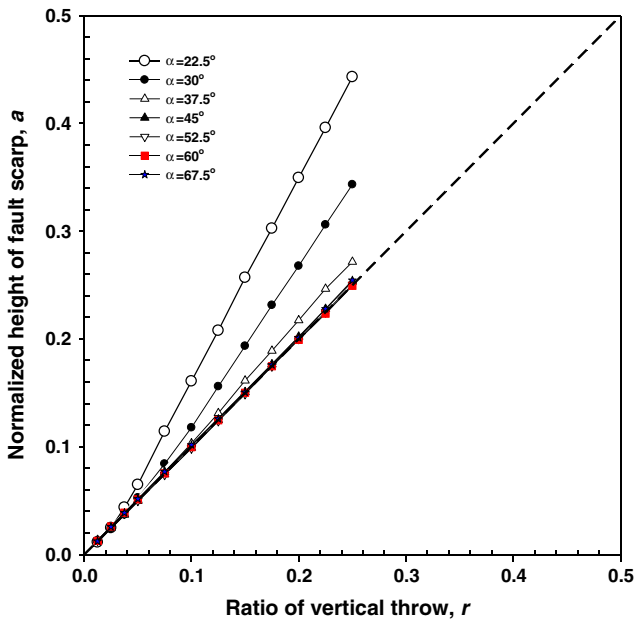


Fig. 23. Relations of the normalized scarp height and the ratio of vertical throw (units not by percent) at various dip angles.

sigmoid function was chosen to describe the normalized surface deformation profiles obtained from the numerical simulation and from the centrifuge experiment. The Gompertz sigmoid function,  $y$ , and its first derivative,  $y'$ , plotted in the proposed coordinate system, are presented in Fig. 18 and are defined as

$$y = y_0 + ae^{-e^{-\frac{x-x_0}{b}}} \quad (10)$$

The first derivative of the Gompertz function,  $y'$ , is

$$y' = \frac{a}{b} \left[ e^{-e^{-\frac{x-x_0}{b}}} \right] e^{-\left(\frac{x-x_0}{b}\right)} \quad (11)$$

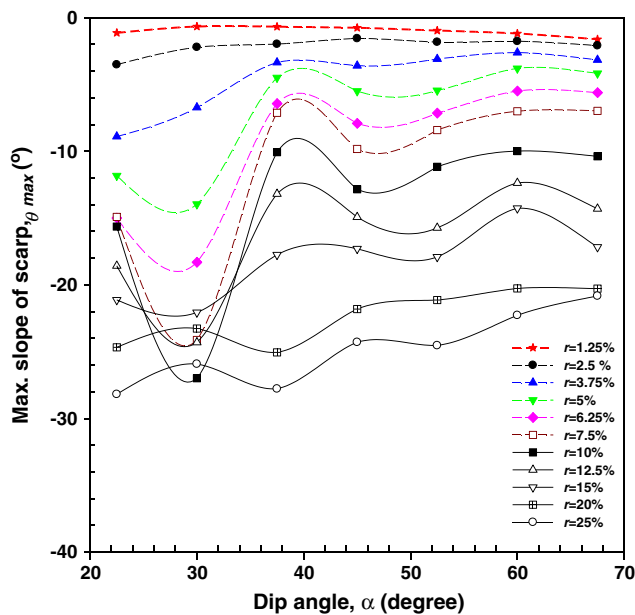


Fig. 24. Relations of the maximum slope of scarp and the ratio of vertical throw at various dip angles.

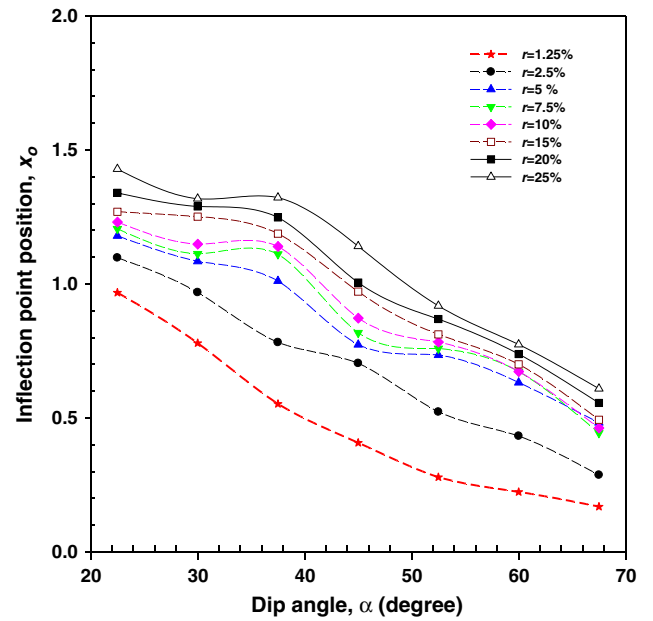


Fig. 25. Relations of the position of inflection point and the different dip angles at various ratios of throw.

where

- $x$  the normalized horizontal distance from the fault tip,  $(d/H)$ ;
- $y$  the normalized uplift height,  $s/H$ , of the ground surface deformation at a normalized horizontal distance  $x$ ,  $(d/H)$ ;
- $y'$  the slope on the ground surface deformation profile at a normalized horizontal distance  $x$ ,  $(d/H)$ ;
- $y_0$  the lower asymptote, the normalized elevation of the original ground surface (we set  $y_0 = 0$  in the study);
- $x_0$  the normalized horizontal distance between the inflection point of the Gompertz curve and the fault tip ( $x = 0$ ) and  $y = a/e$  if  $x = x_0$ ;

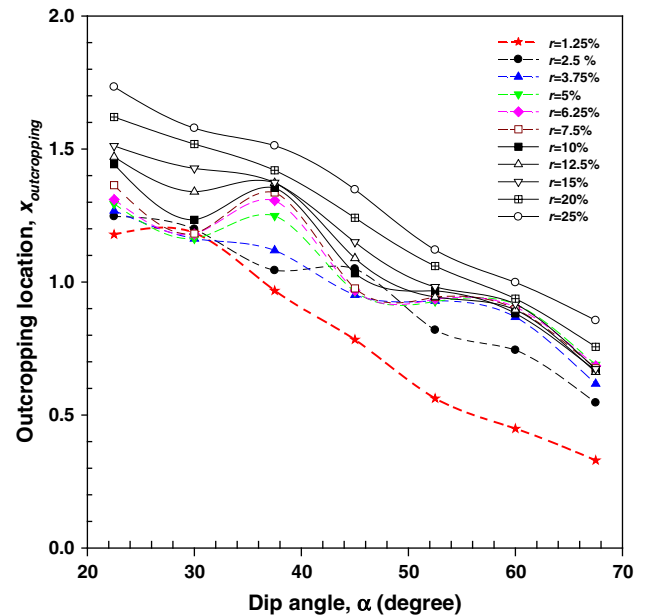


Fig. 26. Relations of the fault normalized outcropping locations and the different dip angles at various ratios of throw.

**Table 3a**Calculated values of  $x_1$  at different dip angles and different throw ratios.

| $\alpha$ (°) | $r$ (%) |        |        |        |        |        |        |        |        |        |        |        |        |
|--------------|---------|--------|--------|--------|--------|--------|--------|--------|--------|--------|--------|--------|--------|
|              | 1.25    | 2.5    | 3.75   | 5      | 6.25   | 7.5    | 10     | 12.5   | 15     | 17.5   | 20     | 22.5   | 25     |
| 22.5         | 0.558   | 0.629  | 0.754  | 0.680  | 0.593  | 0.466  | 0.231  | 0.123  | 0.027  | −0.034 | −0.120 | −0.176 | −0.211 |
| 30           | 0.269   | 0.349  | 0.608  | 0.725  | 0.734  | 0.753  | 0.699  | 0.553  | 0.352  | 0.195  | 0.110  | 0.055  | −0.051 |
| 37.5         | 0.023   | 0.112  | 0.156  | 0.191  | 0.296  | 0.231  | 0.230  | 0.227  | 0.288  | 0.329  | 0.349  | 0.301  | 0.303  |
| 45           | −0.132  | −0.086 | 0.033  | 0.084  | 0.132  | 0.148  | 0.153  | 0.107  | 0.112  | 0.145  | 0.106  | 0.141  | 0.071  |
| 52.5         | −0.211  | −0.207 | −0.109 | 0.035  | 0.044  | 0.010  | −0.017 | 0.012  | −0.018 | −0.066 | −0.090 | −0.102 | −0.131 |
| 60           | −0.226  | −0.327 | −0.345 | −0.288 | −0.215 | −0.207 | −0.216 | −0.253 | −0.310 | −0.252 | −0.251 | −0.271 | −0.365 |
| 67.5         | −0.211  | −0.393 | −0.431 | −0.441 | −0.435 | −0.456 | −0.417 | −0.360 | −0.376 | −0.425 | −0.444 | −0.570 | −0.630 |

- $b$  the growth rate, where the negative value represents the shape of the curve that defines the upper asymptote as it descends to the lower asymptote from the left to the right (smaller  $b$  values provide larger growth rates);
- $a$  the upper asymptote, the maximum normalized uplift height of the ground surface at the hanging wall after reverse faulting;
- $e$  2.7183.

After fitting the Gompertz curve to the data points corresponding to the normalized surface deformation profile measured from the centrifuge experiment (or calculated from the numerical simulations), three parameters ( $x_0$ ,  $a$ , and  $b$ ) were obtained. The normalized surface deformation profiles and the slopes of the profiles predicted using the Gompertz function at different throws were defined in terms of Eqs. (10) and (11). Figs. 19 and 20 show excellent agreement between the experimentally derived (from the centrifuge experiment) normalized surface deformation profiles and their slopes for a 60° dip angle reverse faulting event and the theoretical prediction based on the Gompertz function obtained from the numerical simulations. The utility of the Gompertz function for predicting the normalized surface deformation profiles and their slopes was verified. Here, the value of  $a$  is defined as the normalized height of the fault scarp, according to the characteristic of the Gompertz function, as shown in Fig. 18. Substituting  $x_0$  into Eq. (11) gives the maximum slope of the scarp,  $\theta_{max}$ , at the inflection point,

$$\theta_{max} = \tan^{-1} \frac{a}{eb}. \quad (12)$$

The location of the normalized fault outcropping ( $x_{outcropping}$ ) on the ground surface is another issue that must be considered. We define the location of the normalized fault outcropping,  $x_{outcropping}$ , as shown in Fig. 18, that is

$$x_{outcropping} = x_0 + |b|. \quad (13)$$

The normalized scarp height of a reverse fault,  $a$ , the maximum scarp slope,  $\theta_{max}$ , and the location of a normalized fault outcropping,  $x_{outcropping}$ , are very useful indicators for describing the characteristics of the normalized surface deformation profile induced by reverse faulting in engineering practice. Table 2 lists the characteristic

**Table 3b**Calculated values of  $x_2$  at different dip angles and different throw ratios.

| $\alpha$ (°) | $r$ (%) |       |       |       |       |       |       |       |       |       |       |       |       |
|--------------|---------|-------|-------|-------|-------|-------|-------|-------|-------|-------|-------|-------|-------|
|              | 1.25    | 2.5   | 3.75  | 5     | 6.25  | 7.5   | 10    | 12.5  | 15    | 17.5  | 20    | 22.5  | 25    |
| 22.5         | 1.218   | 1.329 | 1.345 | 1.390 | 1.423 | 1.506 | 1.631 | 1.683 | 1.747 | 1.796 | 1.890 | 1.984 | 2.039 |
| 30           | 1.139   | 1.299 | 1.248 | 1.235 | 1.259 | 1.253 | 1.319 | 1.463 | 1.592 | 1.695 | 1.740 | 1.775 | 1.839 |
| 37.5         | 0.923   | 1.142 | 1.246 | 1.401 | 1.456 | 1.501 | 1.530 | 1.547 | 1.548 | 1.559 | 1.589 | 1.661 | 1.703 |
| 45           | 0.778   | 1.154 | 1.073 | 1.094 | 1.092 | 1.098 | 1.173 | 1.237 | 1.312 | 1.335 | 1.416 | 1.471 | 1.551 |
| 52.5         | 0.589   | 0.933 | 1.062 | 1.055 | 1.074 | 1.09  | 1.123 | 1.092 | 1.142 | 1.214 | 1.240 | 1.268 | 1.319 |
| 60           | 0.494   | 0.853 | 1.015 | 1.082 | 1.065 | 1.063 | 1.054 | 1.077 | 1.110 | 1.098 | 1.129 | 1.149 | 1.215 |
| 67.5         | 0.379   | 0.658 | 0.759 | 0.849 | 0.845 | 0.844 | 0.826 | 0.820 | 0.834 | 0.895 | 0.946 | 1.040 | 1.090 |

parameters of the normalized surface deformation profile at different dip angles and in the case of  $r = 25\%$ .

### 5. Parametric study of the surface deformation profiles induced by reverse faulting along different dip angles

Having validated the proposed PFC<sup>2D</sup> numerical modeling methodology, we performed a series of parametric studies of reverse faulting at dip angles of  $\alpha = 22.5^\circ, 30^\circ, 37.5^\circ, 45^\circ, 52.5^\circ, 60^\circ$ , and  $67.5^\circ$  and at different ratios of throw ( $r = 0.25\%–25\%$ ). In total, 20 normalized ground surface deformation profiles at different ratios of throw for each dip angle were obtained. The Gompertz function associated with a set of parameters ( $a$ ,  $b$ , and  $x_0$ ) was used to describe each normalized ground surface deformation profile calculated from the numerical models. Fig. 21(a) and (b) show the predicted normalized surface deformation profiles and the predicted slopes of the profiles, respectively, at different dip angles in the case of  $r = 25\%$ . The normalized height of the scarp increased as the dip angle decreased for  $\alpha < 45^\circ$ . By contrast, the normalized height of scarp remained unchanged for  $\alpha > 45^\circ$ , as shown in Fig. 21(a). The location of the inflection point,  $x_0$ , moved toward the footwall, and the maximum slope of the scarp increased as  $\alpha$  decreased, as shown in Fig. 21(b).

The two displacement components induced by the fault slip (vertical uplift and horizontal displacement toward the footwall) contributed to the surface and subsurface deformations. The horizontal displacement and the vertical uplift played equal roles in the surface deformation profile in the case of a 45° dip reverse faulting event. For  $\alpha > 45^\circ$ , the vertical uplift was the most significant displacement component, whereas for  $\alpha < 45^\circ$  the horizontal displacement (lateral squeeze or lateral compression) was the most significant. Lateral compression caused passive failure along the plane, which formed an angle of  $45^\circ - 1/2\phi$  with the horizontal ( $\phi =$  friction angle of the soil) along the backfill of the wall. For most soils, the friction angle was approximately  $33^\circ–43^\circ$ , and the passive failure planes formed an angle of  $23^\circ–29^\circ$  with the horizontal. The dip thrust plane coincided with the passive failure plane once the dip angle of the reverse faulting event reached angles of  $23^\circ–29^\circ$ . By comparison, the forced displacement of the hanging wall along the dip angles, which are much smaller than  $23^\circ–29^\circ$ , produced a large lateral compression that could induce displacements along the plane through an angle of  $45^\circ - 1/2\phi$ .

Fig. 22 shows the relationship between the normalized scarp height,  $a$ , and the dip angle,  $\alpha$ , at various ratios of the vertical throw,  $r$ .

**Table 4**  
Calculated values of  $x_{affected}$  at different dip angles and different throw ratios.

| $\alpha$ (°) | $r$ (%) |      |      |      |      |      |      |      |      |      |      |      |      |
|--------------|---------|------|------|------|------|------|------|------|------|------|------|------|------|
|              | 1.25    | 2.5  | 3.75 | 5    | 6.25 | 7.5  | 10   | 12.5 | 15   | 17.5 | 20   | 22.5 | 25   |
| 22.5         | 0.66    | 0.7  | 0.6  | 0.71 | 0.83 | 1.04 | 1.4  | 1.56 | 1.72 | 1.83 | 2.01 | 2.16 | 2.25 |
| 30           | 0.87    | 0.95 | 0.64 | 0.51 | 0.52 | 0.5  | 0.62 | 0.91 | 1.24 | 1.5  | 1.63 | 1.72 | 1.89 |
| 37.5         | 0.9     | 1.03 | 1.09 | 1.21 | 1.16 | 1.27 | 1.3  | 1.32 | 1.26 | 1.23 | 1.24 | 1.36 | 1.4  |
| 45           | 0.91    | 1.24 | 1.04 | 1.01 | 0.96 | 0.95 | 1.02 | 1.13 | 1.2  | 1.19 | 1.31 | 1.33 | 1.48 |
| 52.5         | 0.8     | 1.14 | 1.17 | 1.02 | 1.03 | 1.08 | 1.14 | 1.08 | 1.16 | 1.28 | 1.33 | 1.37 | 1.45 |
| 60           | 0.72    | 1.18 | 1.36 | 1.37 | 1.28 | 1.27 | 1.27 | 1.33 | 1.42 | 1.35 | 1.38 | 1.42 | 1.58 |
| 67.5         | 0.59    | 1.05 | 1.19 | 1.29 | 1.28 | 1.3  | 1.25 | 1.18 | 1.21 | 1.32 | 1.39 | 1.61 | 1.72 |

As expected, larger throw ratios produced higher scarps. Reverse faulting with a small dip angle ( $\alpha < 45^\circ$ ) produced higher scarps for a given throw ratio. By contrast, the scarp height remained constant for  $\alpha > 45^\circ$ . Fig. 23 shows the relationship between the normalized scarp height and the vertical throw ratio (note that the units of the horizontal axis are not percentages in this figure) at various dip angles. The dashed line in the figure indicates that a unit uplift of bedrock produced a vertical displacement with a height equal to that of a fault scarp. The portion of the normalized scarp height that exceeded the vertical throw was attributed to lateral squeezing at lower dip angles ( $\alpha < 45^\circ$ ) during reverse faulting. Fig. 24 shows the relationship between the maximum slope,  $\theta_{max}$ , and the ratio of the vertical throw at various dip angles. A lower dip thrust produced a slightly steeper maximum scarp slope as  $\theta_{max}$  reached a maximum in the case of a dip angle of  $\alpha = 30^\circ$  and  $r = 5\%–12.5\%$ . This observation may result from the fact that the dip angle approximately coincided with the passive failure plane ( $25^\circ$  with respect to the horizontal, for the test sand with a friction angle of  $41^\circ$ ). In summary, a low dip thrust produced a high fault scarp and a slightly steeper scarp slope. Fig. 25 shows the trend in the inflection point position,  $x_o$ , and the dip angle at various throw ratios. Fig. 26 shows the relationship between the normalized fault outcropping location,  $x_{outcropping}$ , and the dip angle, at various throw ratios. As shown in these two figures, a low dip thrust angle are associated with movement of both the inflection point position,  $x_o$ , and the normalized fault outcropping location,  $x_{outcropping}$ , toward the footwall. The values of  $x_o$  and  $x_{outcropping}$  increased with the vertical throw ratio, except in the case of a  $30^\circ$  dip angle reverse faulting event for  $r = 5\%–12.5\%$ .

**6. Establishing affected widths of reverse faulting with different dip angles and at different throws**

The setbacks were recommended to minimize the potential for surface fault rupture that could damage civil structures. Allowable settlement criteria and limiting angular distortions are recommended in the Taiwan Building Codes for use in engineering design practice. Buildings that experienced an angular distortion of 1/150 would be expected to suffer considerable structure damage. In this study, we defined the extent to which a surface deformation profile slope exceeding 1/150 could affect the width of the reverse fault. This criterion provides an indicator for foundation designers to evaluate the safety of a building located near a reverse fault.

Eq. (11) provides the slope of the normalized surface deformation profile,  $y'$ , at the selected normalized horizontal distance,  $x$ , from the fault tip on the bedrock. By setting the slope to 1/150, the values of  $x_1$  (positive or negative) and  $x_2$  (positive) may be calculated, as shown in Fig. 18. The value of  $|x_1|$  is the normalized distance from the left margin of the normalized affected width to the position of the fault tip. The value of  $x_2$  is the normalized distance between the right margin of the normalized affected width and the position of the fault tip; therefore, the value  $x_2 - x_1$  is defined as the normalized affected width induced by reverse faulting. After numerically simulating each case (various dip angles and throws) the values of  $x_1$  and  $x_2$  were calculated and are listed in Tables 3a and 3b. The regressed relations of  $x_1$  and  $x_2$  as a

function of the dip angle,  $\alpha$  (°), and the ratio of the vertical throw,  $r$  (%), are given as

$$x_1 = 1.141 - 0.2164r - 0.02481\alpha + 0.01348\alpha r - 4.375 \times 10^{-5}\alpha r^2 + 7.098 \times 10^{-7}\alpha r^3 - 2.447 \times 10^{-4}\alpha r^2 + 1.508 \times 10^{-6}\alpha r^3 \tag{14}$$

$$x_2 = 1.564 + 0.03797r - 0.01991\alpha + 0.001891\alpha r - 1.707 \times 10^{-4}\alpha r^2 + 3.763 \times 10^{-6}\alpha r^3 - 8.855 \times 10^{-7}\alpha r^2 + 4.478 \times 10^{-9}\alpha r^3 \tag{15}$$

The values of  $R^2$  and adjusted  $R^2$  were (0.8627; 0.8344) and (0.9596; 0.9513) in the regressions described by Eqs. (14) and (15), respectively. Finally, the normalized affected width,  $x_{affected}$ , and the affected width,  $L_{affected}$ , are given as

$$x_{affected} = x_2 - x_1 \tag{16 - a}$$

$$L_{affected} = (x_2 - x_1) \times H. \tag{16 - b}$$

Table 4 lists the calculated values of  $x_{affected}$  at different dip angles and different throw ratios. Fig. 27 shows the relationship between the normalized affected width and the dip angle as a function of the

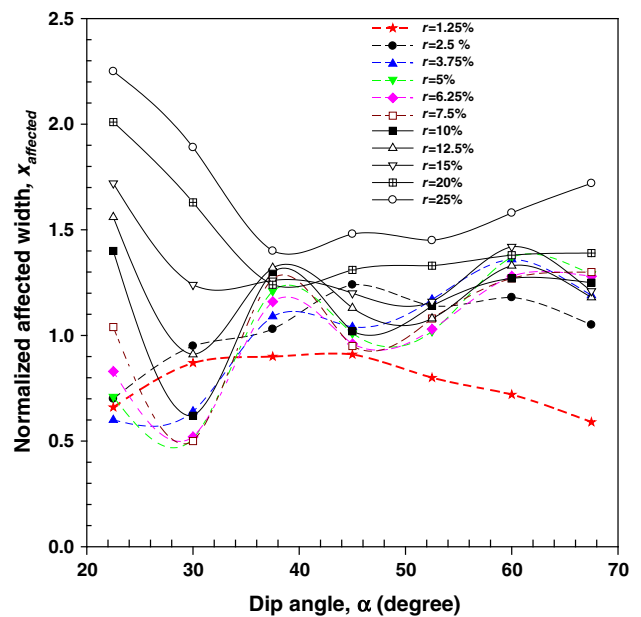
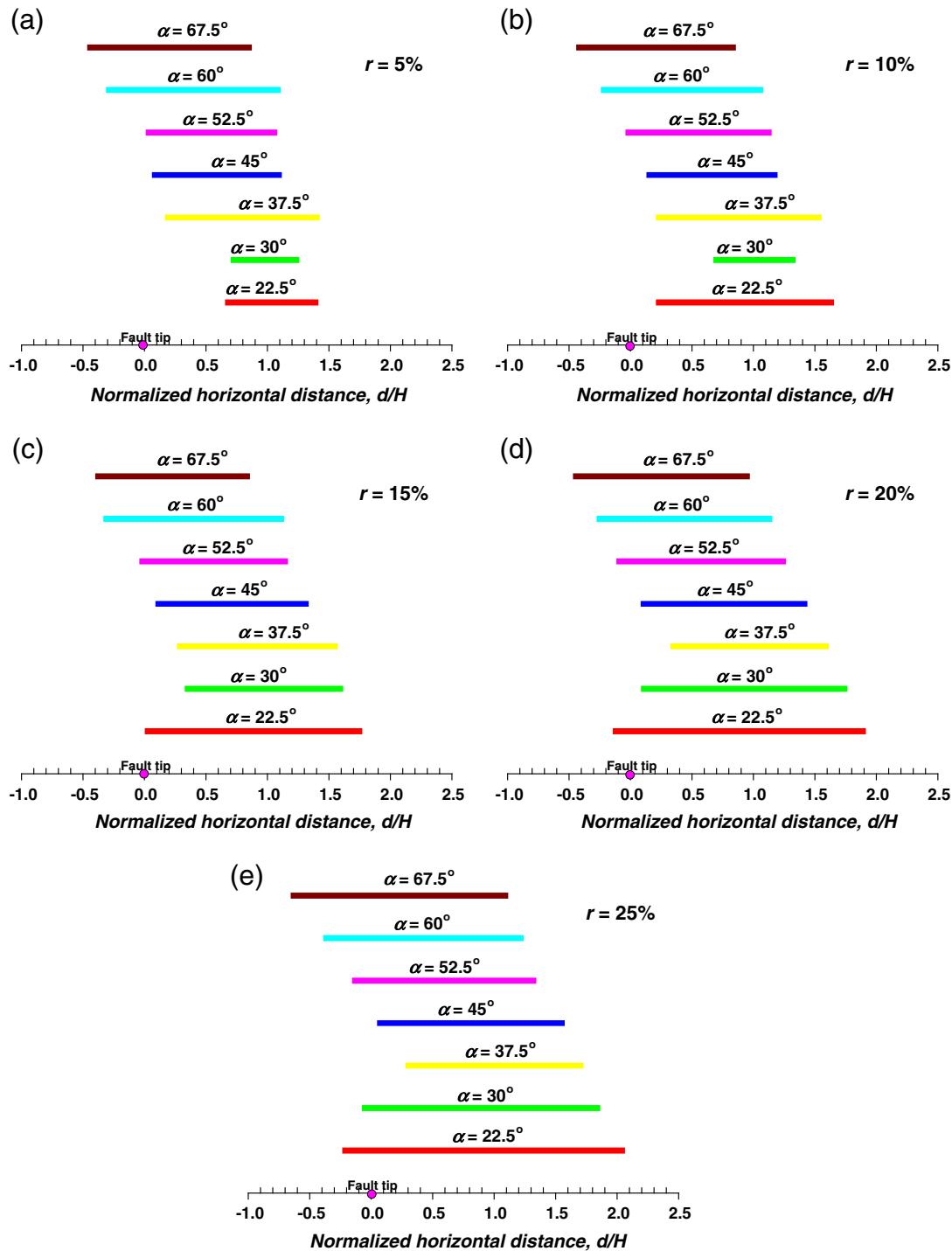


Fig. 27. Relations of the normalized affected width and the different dip angles at various ratios of throw.



**Fig. 28.** Extents of normalized affected width in relation to the position of fault tip those which are induced by different dip reverse faulting at various throw ratios: (a)  $r = 5\%$ ; (b)  $r = 10\%$ ; (c)  $r = 15\%$ ; (d)  $r = 20\%$ ; (e)  $r = 25\%$ .

throw ratio. The  $30^\circ$  dip thrust produced the narrowest normalized affected width for  $r$  between 1.25% and 12.5%; however, for large throw ratios ( $r > 12.5\%$ ), the lower dip thrust developed a wider normalized affected width. Fig. 28(a)–(e) illustrate the extents of the normalized affected width in relation to the position of the fault tips induced by dip reverse faulting events at various throw ratios ( $r = 5\%$ ,  $10\%$ ,  $15\%$ ,  $20\%$ , and  $25\%$ ). These figures provide guidelines that an engineer may use to determine the limits of a zone in which construction should be disallowed or special countermeasures required.

## 7. Subsurface distortion zone as function of the dip of reverse faulting

The particles' coordinate changes and the magnitude of their rotations relative to their original positions in the numerical grain assembly were monitored and traced step by step during the PFC<sup>2D</sup> simulation. This approach provided an understanding of how fault rupture is propagated and permitted us to define the extent of the subsurface distortion zone. Three types of plot were constructed to demonstrate the

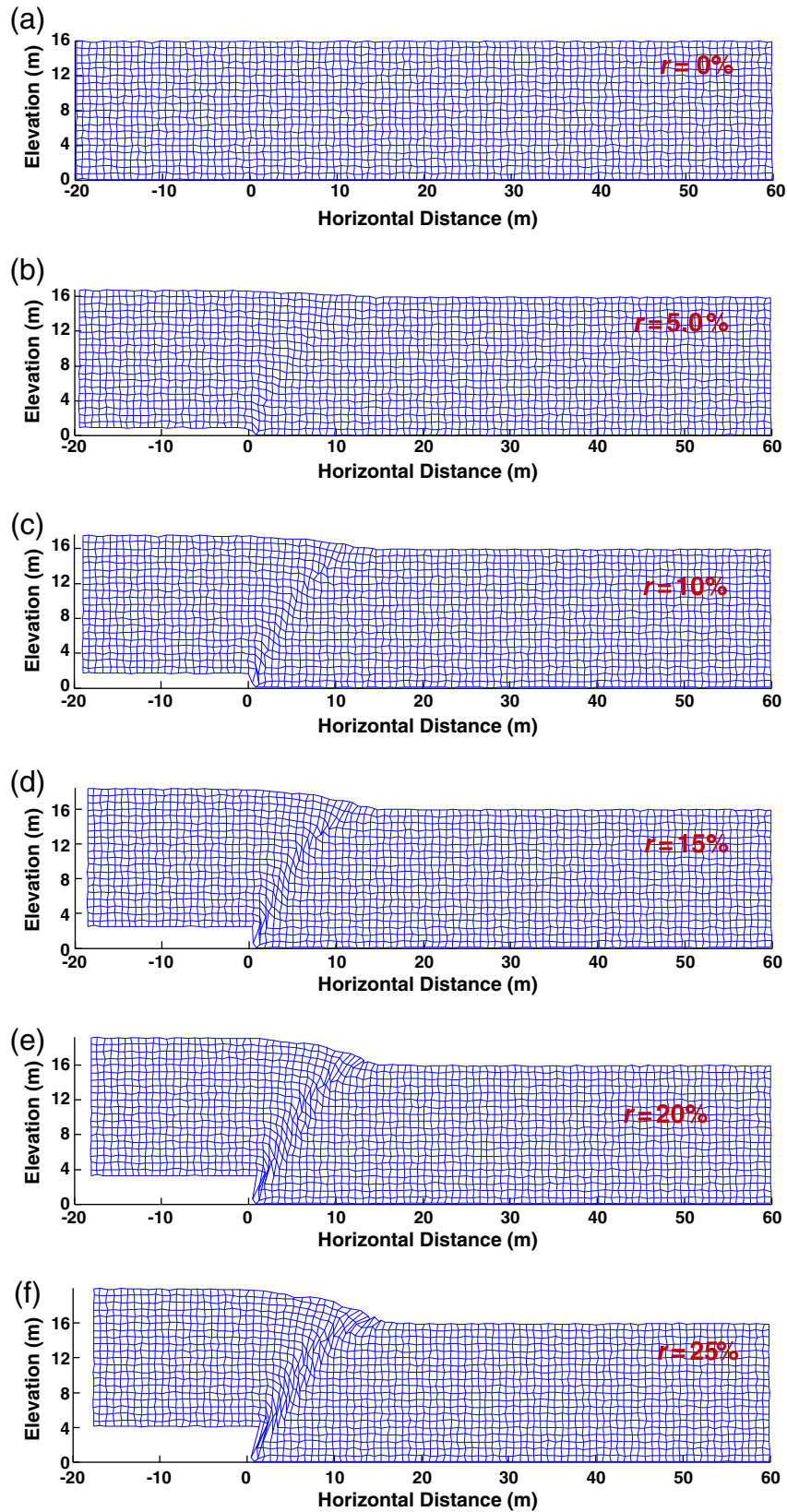


Fig. 29. Evolution of distorted meshes at various throw ratios: (a)  $r = 0\%$ ; (b)  $r = 5\%$ ; (c)  $r = 10\%$ ; (d)  $r = 15\%$ ; (e)  $r = 20\%$ ; (f)  $r = 25\%$ .

evolution of the extent of subsurface distortion zone based on the PFC<sup>2D</sup> numerical simulation results: a plot of the distorted meshes, a plot of the incremental rotation angles of particles, and a plot of the incremental vertical displacements of particles (Chang, 2013). Fig. 29(a)–(f) show

the evolution of the distorted meshes for a 16 m thick soil bed subjected to a 60° dip angle reverse faulting for  $r = 0\%$ –25%. The geometry of the mesh gradually distorted as the vertical throw increased. The extent and shape of the distorted zone at  $r = 25\%$  agreed well with the results

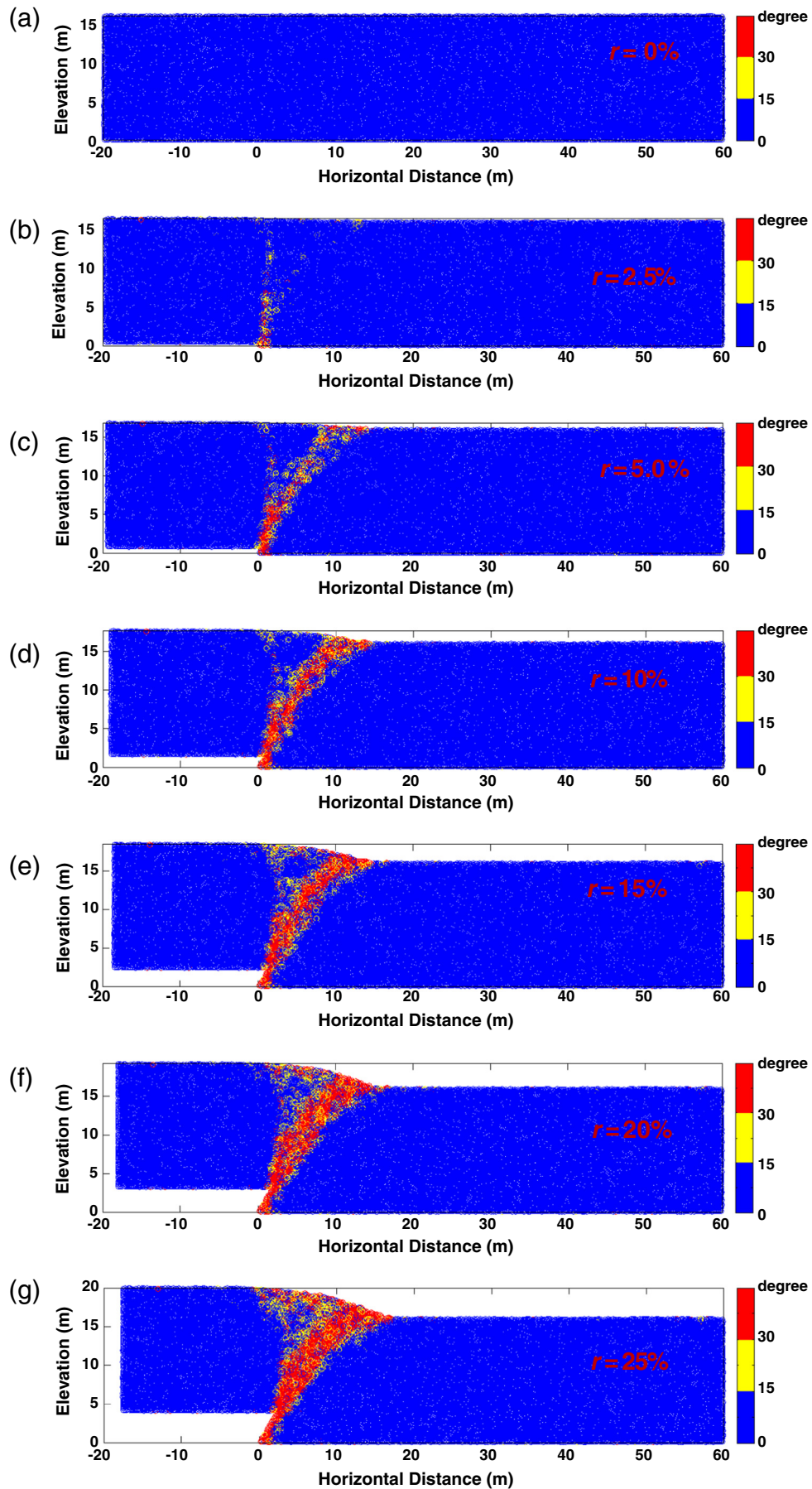


Fig. 30. Evolution of incremental rotation angle magnitude at various throw ratios: (a)  $r = 0\%$ ; (b)  $r = 2.5\%$ ; (c)  $r = 5\%$ ; (d)  $r = 10\%$ ; (e)  $r = 15\%$ ; (f)  $r = 20\%$ ; (g)  $r = 25\%$ .

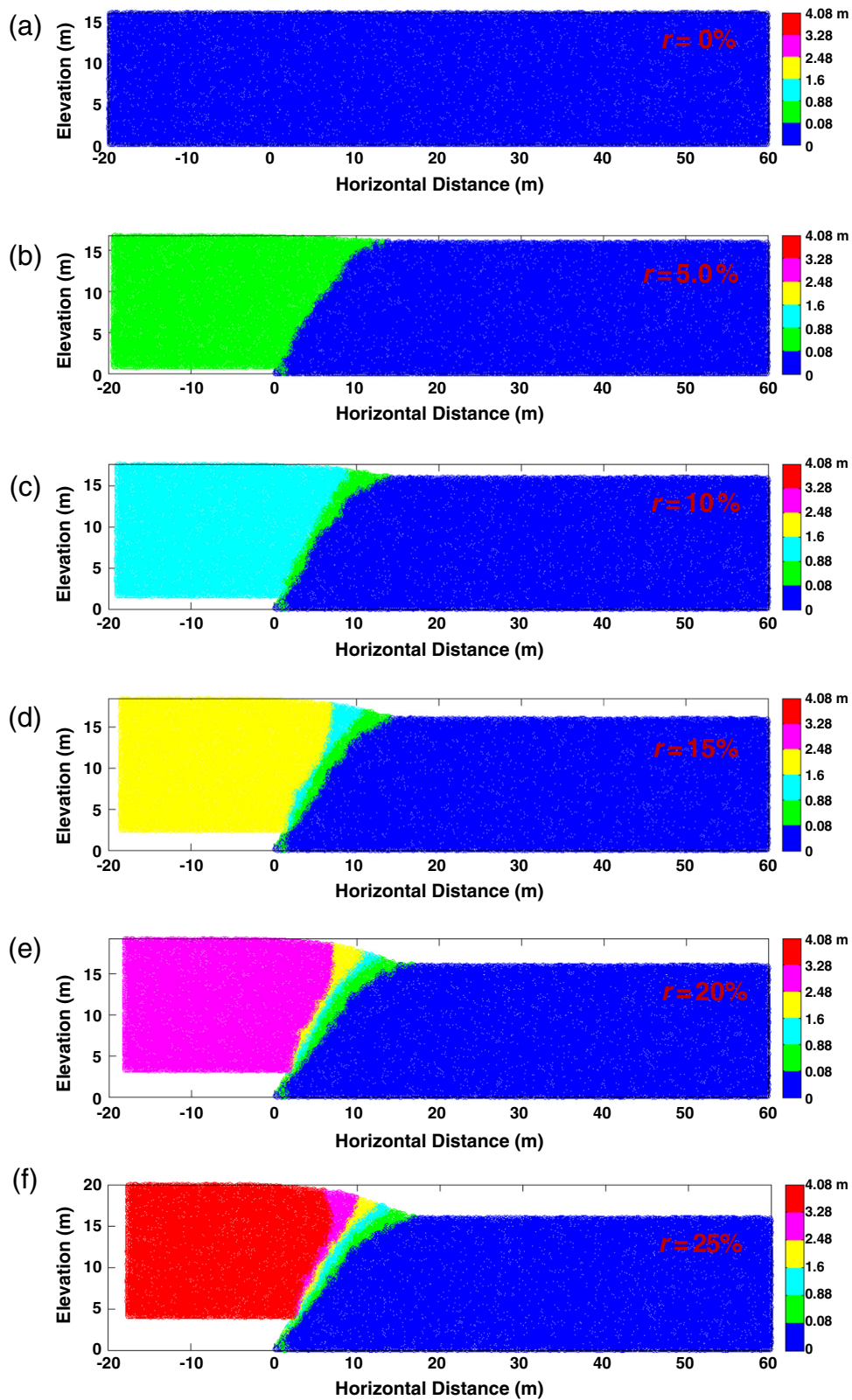


Fig. 31. Evolution of incremental vertical displacement magnitude at various throw ratios: (a)  $r = 0\%$ ; (b)  $r = 5\%$ ; (c)  $r = 10\%$ ; (d)  $r = 15\%$ ; (e)  $r = 20\%$ ; (f)  $r = 25\%$ .

obtained from the centrifuge experiment, as shown in Fig. 10. Figs. 30 and 31 show the fields of incremental rotation angle magnitude and the incremental vertical displacement magnitude after reverse faulting from  $r = 0\%$ – $25\%$ , respectively. The confines of the larger incremental rotation angles shown in Fig. 30 were used to define the subsurface

distortion zone. The initial shear band began at the fault tip and migrated vertically upwards to the surface (Figure 30(b)). Thereafter, the second shear band along the dip plane developed and gradually bent over the footwall so that the rupture became gentler as it approached the surface. The vertical throw required for the shear

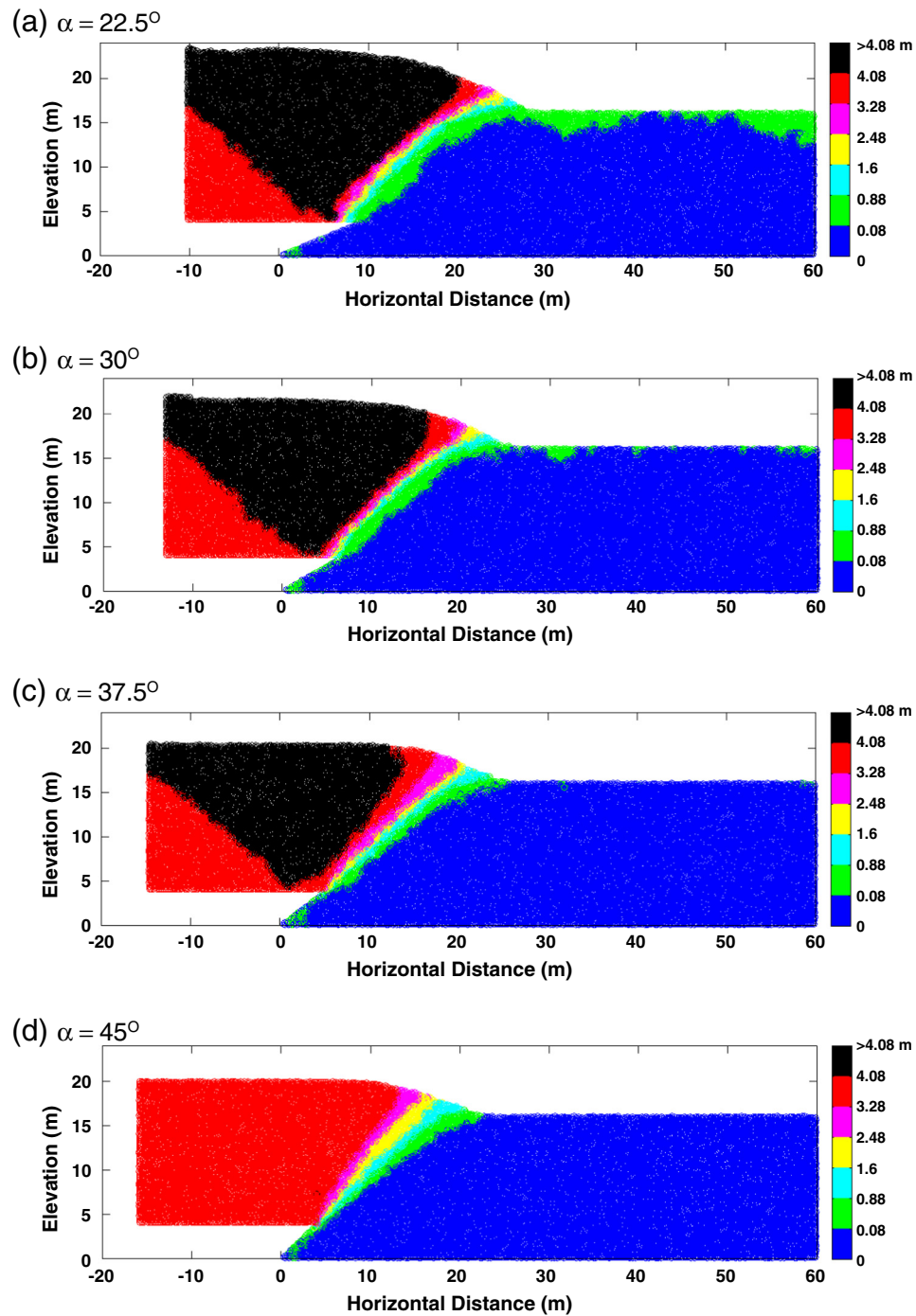


Fig. 32. Surface distortion zone observed by the incremental vertical displacement magnitude at the ratio of vertical throw  $r = 25\%$ ; (a)  $\alpha = 22.5^\circ$ ; (b)  $\alpha = 30^\circ$ ; (c)  $\alpha = 37.5^\circ$ ; (d)  $\alpha = 45^\circ$ ; (e)  $\alpha = 52.5^\circ$ ; (f)  $\alpha = 60^\circ$ ; (g)  $\alpha = 67.5^\circ$ .

band to form an outcrop is important for the design of structures that overlay an active fault. A comparison between Fig. 30(a) and (b) suggests that the required vertical throw for fault outcropping may be  $r = 1.25\%$ – $2.5\%$ . Although the vertical throw increased, the width of the shear band did not increase, even after  $r$  reached 25%. Similarly, the extents to which the incremental vertical displacements varied prominently (rapid changes are shown in color), as shown in Fig. 31, were useful for defining the subsurface distorted zone. These three different plots all indicated similar geometries and shapes for the subsurface distorted zones.

Fig. 32 shows the subsurface distortion zones identified under incremental vertical displacement magnitudes with a vertical throw ratio of  $r = 25\%$  for a reverse faulting event with different dip angles ( $\alpha = 22.5^\circ, 30^\circ, 37.5^\circ, 45^\circ, 52.5^\circ, 60^\circ, 67.5^\circ$ ). As described in the previous section, the horizontal displacement (lateral compression) played a significant role at lower dip thrusts ( $\alpha = 22.5^\circ, 30^\circ, 37.5^\circ$ ). A back-thrust fault developed under such circumstances. The back-thrust fault combined with the major shear band to form an inverted triangle wedge (the black area in Fig. 32(a)–(c)). This kinematic mechanism significantly contributed to the uplift on the hanging

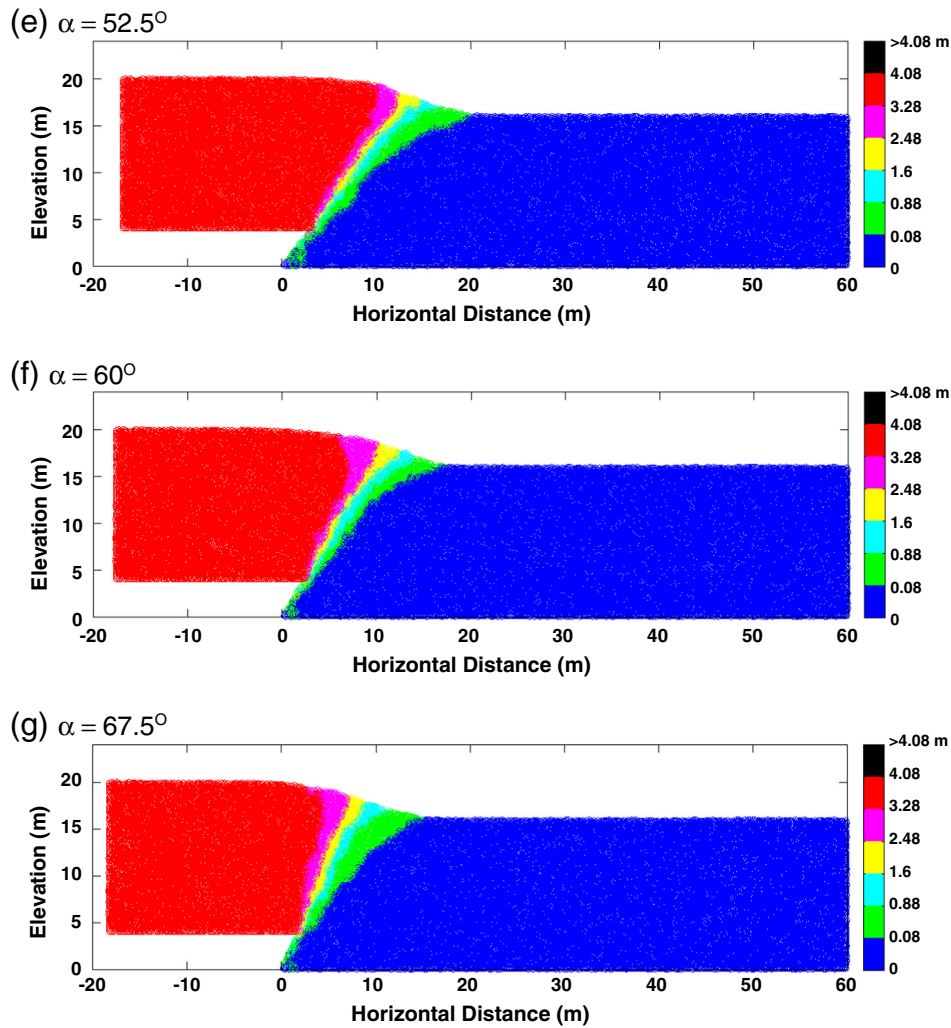


Fig. 32 (continued).

wall and increased the scarp height, as shown in Fig. 22. No back-thrust fault appeared on the hanging wall, even for  $r = 25\%$  in the cases of  $\alpha \geq 45^\circ$ .

## 8. Conclusions

The 2D distinct element method was used to investigate the propagation of fault rupture traces through overlying sand during reverse faulting along different dip angles and at different vertical throws. The micromechanical material parameters calibrated based on centrifuge experimental results were used in the numerical simulation. The results of the centrifuge modeling and numerical simulation efforts led to the following conclusions:

- (1) The numerical simulations were validated by comparison to the results obtained from the centrifuge experiments. The predictions of both the surface deformation profiles and the subsurface distortion zones for a 16 m thick soil bed subjected to a  $60^\circ$  dip angle reverse faulting from  $r = 0.25\text{--}25\%$  were accurate relative to the experimental results, which provides confidence in the results obtained from numerical simulations of reverse faulting along different dip angles and at different vertical throws.
- (2) The Gompertz sigmoid function provided a good fit to the normalized surface deformation profiles obtained from both the numerical simulations and from the centrifuge experiments. The utility of a Gompertz function with three parameters ( $a$ ,  $b$ , and  $x_0$ ) for the prediction of a normalized surface deformation profile and slope was verified. The three parameters associated with the characteristics of the Gompertz function (the normalized scarp height, the maximum scarp slope, and the location of the normalized fault outcropping) were clearly defined. A slope of  $1/150$  on the surface deformation profile was identified as a useful criterion for determining the distance from the fault, the normalized affected width, and the location relative to the fault tip on the base rock. The relationship between the normalized affected width, the dip angle, and the throw ratio was described, and guidelines for specifying the widths of setback zones were provided.
- (3) The dip significantly affected the kinematic mechanism underlying the reverse faulting event. For a given vertical throw, the scarp height increased as the dip angle decreased for  $\alpha < 45^\circ$ , and the scarp height remained constant for  $\alpha > 45^\circ$ . As the dip angle decreased, the location of the fault outcropping moved toward the footwall and the maximum scarp slope increased.
- (4) The horizontal displacement played a significant role in the low dip thrusts ( $\alpha = 22.5^\circ, 30^\circ, 37.5^\circ$ ). A back-thrust fault developed and an inverted triangle wedge formed at the subsurface.

## Acknowledgments

This study was sponsored by the Central Geological Survey (CGS), Ministry of Economic Affairs, Taiwan (100-5226904000-05-01 & 101-5226904000-03-01). The authors would like to express their gratitude for the financial and technical supports, which have made this study and future research possible.

## References

- 921 Earthquake Museum of Taiwan, d. <http://www.921emt.edu.tw>.
- Abe, S., Gent, H.V., Urai, J.L., 2011. DEM simulation of normal faults in cohesive materials. *Tectonophysics* 512, 12–21.
- Anastasopoulos, I., Gazetas, G., Bransby, M.F., Davies, M.C.R., Nahas, E.L., 2007. Fault rupture propagation through sand: finite-element analysis and validation through centrifuge experiments. *J. Geotech. Geoenviron. Eng.* 133 (8), 943–958.
- Anastasopoulos, I., Gerolymos, N., Gazetas, G., Bransby, M.F., 2008. Simplified approach for design of raft foundations against fault rupture. Part I: free field. *Earthq. Eng. Eng. Vib.* 7 (2), 147–163.
- Anastasopoulos, I., Gazetas, G., Ulusay, R., Aydan, Ö., Hamada, M., 2001. The Behavior of Structures Built on Active Fault Zones: Examples from the Recent Earthquakes in Turkey. *Seismic Fault-induced Failures*, pp. 1–26.
- Borchardt, G., 2010. Establishing appropriate setback widths for active faults. *Environ. Eng. Geosci.* 16 (1), 47–53.
- Bransby, M.F., Davies, M.C.R., EL Nahas, A., 2008a. Centrifuge modeling of normal fault–foundation interaction. *Bull. Earthq. Eng.* 6 (4), 585–605.
- Bransby, M.F., Davies, M.C.R., EL Nahas, A., Nagaoka, S., 2008b. Centrifuge modeling of reverse fault–foundation interaction. *Bull. Earthq. Eng.* 6 (4), 607–628.
- Bray, J.D., Seed, R.B., Cluff, L.S., Seed, H.B., 1994a. Earthquake fault rupture propagation through soil. *J. Geotech. Eng.* 120 (3), 543–561.
- Bray, J.D., Seed, R.B., Seed, H.B., 1994b. Analysis of earthquake fault rupture propagation through cohesive soil. *J. Geotech. Eng.* 120 (3), 562–580.
- Bryant, W., Hart, E.W., 2007. Alquist-Priolo Earthquake Fault Zoning Act with Index to Earthquake Fault Zones Maps. California Department of Conservation, Interim Revision.
- Chang, Y.Y., 2013. Use of Centrifuge Modeling and Distinct Element Method to Evaluate the Surface and Subsurface Deformation of Normal Faulting and Reverse Faulting PhD Dissertation National Central University, Taiwan.
- Chang, Y.Y., Lee, C.J., Huang, W.C., Huang, W.J., Lin, M.L., Hung, W.Y., Line, Y.H., 2013. Use of centrifuge experiments and discrete element analysis to model the reverse fault slip. *Int. J. Civ. Eng.* 11 (2), 79–89.
- Chen, C.C., Huang, C.T., Cherng, R.H., Jeng, V., 2000. Preliminary investigation of damage to near fault buildings of the 1999 Chi-Chi earthquake. *Earthq. Eng. Eng. Seismol.* 2 (1), 79–92.
- Chen, W.S., Yang, C.C., Yen, I.C., Lee, L.S., Lee, K.J., Yang, H.C., Ota, Y., Lin, C.W., Lin, W.H., Shih, T.S., Lu, S.T., 2007. Late Holocene paleoseismicity of the southern part of the Chelungpu Fault in Central Taiwan: evidence from the Chushan excavation site. *Bull. Seismol. Soc. Am.* 97 (1B), 1–13.
- Cole Jr., D.A., Lade, P.V., 1984. Influence zones in alluvium over dip-slip faults. *J. Geotech. Eng. ASCE* 110 (5), 599–615.
- Cundall, P.A., Strack, O.D.L., 1979. A discrete numerical model for granular assemblies. *Geotechnique* 29 (1), 47–65.
- Dong, J.J., Wang, C.D., Lee, C.T., Liao, J.J., Pan, Y.W., 2004. The influence of surface ruptures on building damage in the 1999 Chi-Chi earthquake: a case study in Fengyuan City. *Eng. Geol.* 71 (2), 157–179.
- Fadaee, M., Jafari, M.K., Kamalian, M., Shafiee, A., Mossavi, S.M., 2013. Feasibility study of fault rupture deviation by slurry wall. *Int. J. Civ. Eng.* 11 (2), 90–99.
- Lee, C.J., Wang, C.R., Wei, Y.C., Hung, W.Y., 2011. Evolution of the shear wave velocity during shaking modeled in centrifuge shaking table tests. *Bull. Earthq. Eng.* 10 (2), 401–420.
- Lin, M.L., Lu, C.Y., Chang, K.J., Jeng, F.F., Lee, C.J., 2005. Sandbox experiments of plate convergence-scale effect and associated mechanism. *Terr. Atmos. Ocean. Sci.* 16 (3), 595–620.
- Lin, M.L., Chung, C.F., Jeng, F.S., 2006. Deformation of overburden soil induced by thrust fault slip. *Eng. Geol.* 88, 70–89.
- Lin, M.L., Chung, C.F., Jeng, F.S., 2007. The deformation of overburden soil induced by thrust faulting and its impact on underground tunnels. *Eng. Geol.* 92, 110–132.
- Loukidis, D., Bouckovalas, G., Papadimitriou, A., 2009. Analysis of fault rupture propagation through uniform soil cover. *Soil Dyn. Earthq. Eng.* 29, 1389–1404.
- Mortazavi Zanjani, M., Soroush, A., 2013. Numerical modeling of reverse fault rupture propagation through clayey embankment. *Int. J. Civ. Eng.* 11 (2), 1221–1232.
- Ng, C.W.W., Cai, Q.P., Hu, P., 2012. Centrifuge and numerical modeling of normal fault-rupture propagation in clay with and without a preexisting fracture. *J. Geotech. Geoenviron. Eng. ASCE* 138 (12), 1492–1502.
- Nollet, S., Kleine Vennekate, G.J., Giesew, S., Vrolijk, P., Urai, J.L., Ziegler, M., 2012. Localization patterns in sandbox-scale numerical experiments above a normal fault in basement. *J. Struct. Geol.* 39, 199–209.
- Taniyama, H., 2011. Numerical analysis of overburden soil subjected to strike-slip fault: distinct element analysis of Nojima fault. *Eng. Geol.* 123 (3), 194–303.
- Yimsiri, S., Soga, K., 2000. Micromechanics-based stress-strain behavior of soils at small strains. *Geotechnique* 50 (1), 559–571.